

# Measurement of the Total Cross Section of the ${}^2\text{H}(\alpha,\gamma){}^6\text{Li}$ Radiative Capture Reaction

## Inauguraldissertation

zur

Erlangung der Würde eines Doktors der Philosophie

vorgelegt der

Philosophisch-Naturwissenschaftlichen Fakultät

der Universität Basel

von

**Giuseppe A. Testa**

aus Basel, BS

Basel, 2010

Originaldokument gespeichert auf dem Dokumentenserver der Universität Basel  
**edoc.unibas.ch**



Dieses Werk ist unter dem Vertrag „Creative Commons Namensnennung-Keine kommerzielle Nutzung-Keine Bearbeitung 2.5 Schweiz“ lizenziert. Die vollständige Lizenz kann unter [creativecommons.org/licences/by-nc-nd/2.5/ch](http://creativecommons.org/licences/by-nc-nd/2.5/ch) eingesehen werden.



Genehmigt von der Philosophisch-Naturwissenschaftlichen Fakultät auf  
Antrag von

Prof. Dr. Bernd Krusche  
PD Dr. Jürg Jourdan  
Prof. Dr. Dr. h.c. Ingo Sick

Basel, den 20. Mai 2008

Prof. Dr. Hans-Peter Hauri

Dekan





## Namensnennung-Keine kommerzielle Nutzung-Keine Bearbeitung 2.5 Schweiz

---

### Sie dürfen:



das Werk vervielfältigen, verbreiten und öffentlich zugänglich machen

### Zu den folgenden Bedingungen:



**Namensnennung.** Sie müssen den Namen des Autors/Rechteinhabers in der von ihm festgelegten Weise nennen (wodurch aber nicht der Eindruck entstehen darf, Sie oder die Nutzung des Werkes durch Sie würden entlohnt).



**Keine kommerzielle Nutzung.** Dieses Werk darf nicht für kommerzielle Zwecke verwendet werden.



**Keine Bearbeitung.** Dieses Werk darf nicht bearbeitet oder in anderer Weise verändert werden.

- Im Falle einer Verbreitung müssen Sie anderen die Lizenzbedingungen, unter welche dieses Werk fällt, mitteilen. Am Einfachsten ist es, einen Link auf diese Seite einzubinden.
- Jede der vorgenannten Bedingungen kann aufgehoben werden, sofern Sie die Einwilligung des Rechteinhabers dazu erhalten.
- Diese Lizenz lässt die Urheberpersönlichkeitsrechte unberührt.

#### Die gesetzlichen Schranken des Urheberrechts bleiben hiervon unberührt.

Die Commons Deed ist eine Zusammenfassung des Lizenzvertrags in allgemeinverständlicher Sprache: <http://creativecommons.org/licenses/by-nc-nd/2.5/ch/legalcode.de>

#### Haftungsausschluss:

Die Commons Deed ist kein Lizenzvertrag. Sie ist lediglich ein Referenztext, der den zugrundeliegenden Lizenzvertrag übersichtlich und in allgemeinverständlicher Sprache wiedergibt. Die Deed selbst entfaltet keine juristische Wirkung und erscheint im eigentlichen Lizenzvertrag nicht. Creative Commons ist keine Rechtsanwalts-gesellschaft und leistet keine Rechtsberatung. Die Weitergabe und Verlinkung des Commons Deeds führt zu keinem Mandatsverhältnis.



At first, in order to retain an old custom, I would like to thank many people whose support and help with my thesis have been of value to me.

It was a privilege to be part of the DaLi project in the group of Prof. Dr. Dr. h.c. Ingo Sick and Prof. Dr. Bernd Krusche.

For their leading work on the experiment and their support during my PhD study PD Dr. Jürg Jourdan, PD. Dr. Heini Mühry, PD Dr. Daniela Kiselev (nee Rohe) and Daniel Sacker deserve special thanks. They mainly contributed to my education in science.

The final analysis of the measured data has been concluded with the support of Dr. Yury Gusev from Petersburg Nuclear Physics Institute. His dedication to details of the analysis has been of great value and therefore I express my gratitude to him.

For the correction of the draft of the present thesis and the precious discussions I would like to thank Prof. Dr. Dr. h.c. Ingo Sick.

During my research in Basel I appreciated the highly professional work of the mechanic and electronic workshop of the Institute of Physics and therefore many thanks to the team of Sascha Martin and Michael Steinacher.

I am deeply in my parents', "mamma e papà", debt for their support during all my education. To my father who spent thousands of hours with me in the experimental hall and to my mother for supplying us with delicious food, I say thank you.

Last I would like to express my profound gratefulness to my *Bienchen* for having been so patient during the stressful time of the experiment and to my sisters for taking care of my cat.

I hope my beloved cat "Ughur" forgave me for having left her for long periods alone during the data taking of the experiment.

Basel, February 2010





# Contents

0.1	Preface . . . . .	6
0.2	Abstract . . . . .	6
<b>1</b>	<b>Introduction</b>	<b>7</b>
1.1	Big-bang nucleosynthesis . . . . .	7
1.1.1	Nuclear reaction network of ${}^6\text{Li}$ . . . . .	9
1.2	Theoretical and Experimental cross section data of the ${}^2\text{H}(\alpha,\gamma){}^6\text{Li}$ radiative capture reaction . . . . .	11
1.2.1	Theoretical cross section . . . . .	12
<b>2</b>	<b>Experiment</b>	<b>14</b>
2.1	Accelerator . . . . .	14
2.2	Beam line . . . . .	15
2.2.1	Beam energy selection . . . . .	17
2.2.2	Beam chopper . . . . .	17
2.2.3	Faraday cup . . . . .	22
2.3	Cryogenic targets . . . . .	24
2.3.1	Solid $\text{D}_2$ target . . . . .	24
2.3.2	Solid $\text{D}_2\text{O}$ target . . . . .	29
2.4	Detectors . . . . .	30
2.4.1	Cylindrical NaI(Tl) detector . . . . .	31
2.4.2	Silicon diode detector . . . . .	38
2.4.3	Cosmic rays detector . . . . .	40
2.5	Shielding . . . . .	42
2.6	Electronic setup & Signal processing . . . . .	43
2.6.1	RF-signal via pickup coil . . . . .	44
2.6.2	Data acquisition . . . . .	45
<b>3</b>	<b>Data analysis</b>	<b>46</b>
3.1	Beam charge . . . . .	46
3.2	Background reactions . . . . .	49
3.2.1	${}^{16}\text{O}(\alpha,\gamma){}^{20}\text{Ne}$ radiative capture . . . . .	50
3.2.2	Neutron induced background . . . . .	51
3.3	Filtering the data . . . . .	52
3.4	Simulation of the response of the DALI-detector to gamma rays	56
3.5	Comparison of the 2.3 MeV data to simulation . . . . .	58

3.6	Analysis of the data at 1.9, 1.5 and 1.0 MeV . . . . .	60
<b>4</b>	<b>Conclusion</b>	<b>61</b>
<b>A</b>	<b>Schematic setup of the electronics</b>	<b>62</b>
<b>B</b>	<b>Technical Drawings of the DaLi shielding</b>	<b>74</b>
<b>C</b>	<b>Greinacher-style multiplier for the 4 MV accelerator</b>	<b>78</b>
<b>D</b>	<b>Beam line</b>	<b>80</b>
<b>E</b>	<b>Energy dependence of the time spectrum</b>	<b>82</b>

# List of Figures

1.1	BBN, WMAP and observed abundances . . . . .	8
1.2	BBN and WMAP prediction of lithium abundance . . . . .	9
1.3	BBN reaction network . . . . .	10
1.4	Astrophysical S-factor of the ${}^2\text{H}(\alpha,\gamma){}^6\text{Li}$ reaction . . . . .	11
1.5	S-factor for the ${}^2\text{H}(\alpha,\gamma){}^6\text{Li}$ reaction with $E_1$ and $E_2$ . . . . .	12
1.6	Total cross section of the ${}^2\text{H}(\alpha,\gamma){}^6\text{Li}$ reaction . . . . .	13
2.1	Ion source placed on top of the white porcelain acceleration tube . . . . .	14
2.2	High voltage cascade and steel isolation tank . . . . .	15
2.3	Last section of the beam line . . . . .	16
2.4	Analyzer magnet -beam energy selection- . . . . .	17
2.5	Sketch of the beam chopper . . . . .	18
2.6	RF-emitter and chopper barrel . . . . .	19
2.7	Copper plates of the beam chopper . . . . .	19
2.8	Optical beam profile . . . . .	20
2.9	$\alpha$ -C scattering setup . . . . .	20
2.10	$\alpha$ -C detector . . . . .	21
2.11	Time structure of the beam . . . . .	21
2.12	Relative charge measurement . . . . .	22
2.13	Faraday cup . . . . .	23
2.14	Cooling expander . . . . .	25
2.15	Target backing on expander . . . . .	26
2.16	$\text{D}_2$ -gas sprinkler . . . . .	26
2.17	Cryogenic $\text{D}_2$ target (side view) . . . . .	27
2.18	Liquid nitrogen cooled beryllium backing . . . . .	29
2.19	Beryllium backing (back side view) . . . . .	30
2.20	$\text{D}_2\text{O}$ vapor system . . . . .	30
2.21	DaLi-detector view from top . . . . .	31
2.22	Phototube labels . . . . .	32
2.23	Crystal No.2 with Y-88 source . . . . .	33
2.24	Fit of the energy resolution . . . . .	33
2.25	Time vs. energy spectrum of alpha-tritium capture . . . . .	36
2.26	TDC spectrum of alpha-tritium capture . . . . .	37
2.27	Time resolution . . . . .	37
2.28	Silicon detector . . . . .	38

2.29	ADC spectra of silicon detector . . . . .	39
2.30	Paddles of the cosmic rays detector under the shielding housing	40
2.31	Bars of the cosmic rays detector on top of the shielding housing	41
2.32	Measured activity of background in the 4MV experimental hall	42
2.33	Shielding housing in construction . . . . .	43
2.34	Pickup coil and RF-beam chopper coils . . . . .	44
3.1	Schematic setup of the FC calibration . . . . .	46
3.2	FC calibration function . . . . .	47
3.3	Charge calibration of the scaler iris-setup . . . . .	49
3.4	HpGe spectrum of the $\alpha$ -O capture on normal water . . . . .	50
3.5	DaLi spectrum of the $\alpha$ -O capture on normal water . . . . .	51
3.6	Raw ADC spectrum . . . . .	53
3.7	Raw TDC spectrum . . . . .	53
3.8	Energy spectrum of the d- $\alpha$ capture at 2.3 MeV . . . . .	54
3.9	Energy spectrum of neutron background . . . . .	55
3.10	Time dependency of the energy spectrum of the neutron back- ground . . . . .	55
3.11	Simulated response of the DaLi detector . . . . .	58
3.12	Contribution of background and simulation curves to the fit .	59
C.1	Greinacher-style multiplier . . . . .	79
D.1	Beam line, schematic drawing . . . . .	81
E.1	Energy spectrum of channel 8 . . . . .	82
E.2	TDC spectra of the ADC slices 1 to 4 of channel 8 . . . . .	83
E.3	TDC spectra of the ADC slices 5 to 8 of channel 8 . . . . .	84

# List of Tables

2.1	Energy resolution . . . . .	34
2.2	Efficiency of the DaLi-detector at 898 keV and 1836 keV . . .	36
2.3	Beam time accounting . . . . .	45
3.1	Faraday cup calibration . . . . .	47
3.2	Total charge of the experiment and stat. error . . . . .	48
3.3	Simulated photo-peak efficiency . . . . .	56

## 0.1 Preface

The project of the cross section measurement of the  ${}^2\text{H}(\alpha,\gamma){}^6\text{Li}$  started in autumn 2002 and ended with the shutdown of the accelerator in May 2007. The project's name 'DaLi' is an acronym for the involved nuclei in the reaction (deuteron, alpha and  ${}^6\text{Li}$ ). The experiment was carried out in Basel and has been funded by the Swiss National Science Foundation with the support of the Institute of Physics of the University of Basel. The members of the project in the group of Prof. Dr. Ingo Sick and after his retirement of his successor Prof. Dr. Bernd Krusche are PD Dr. Jürg Jourdan, PD Dr. Heini Mühry, Daniel Sacker and myself.

## 0.2 Abstract

Big-bang nucleosynthesis (BBN) calculations of the abundances of the light isotopes  ${}^2\text{H}$ ,  ${}^3\text{He}$ ,  ${}^4\text{He}$  and  ${}^7\text{Li}$  in the universe have been successfully confirmed via observation. For primordial  ${}^6\text{Li}$  a clear detection in low-metallicity objects, which could show a primordial component, is not yet available. Only a theoretical determination of the abundance of  ${}^6\text{Li}$  exists. However these calculations require the experimental measurement of the  ${}^2\text{H}(\alpha,\gamma){}^6\text{Li}$  radiative capture reaction cross section.

At present the value of the reaction cross section at the energies appropriate to the Big-bang temperatures (approx. energy: 50-200 keV) has not been measured directly. The direct measurement is a challenging task since the estimated cross section is in the nano or even sub-nanobarn domain. Additionally the deuterons of the reaction are a strong source of background when they breakup and produce neutrons. Past efforts have avoided this issue by the use of thin gas-targets of deuterium allowing the detection of the recoil  ${}^6\text{Li}$  and hence reconstructing the full reaction channel. The drawback is a loss of luminosity, which is prohibitive at lower energies, where the cross section drops down exponentially.

At the 4MV Cockroft-Walton accelerator in Basel we tried to improve this situation by measuring the total cross section of capture reaction down to a c.m. energy of around 400 keV and demonstrating the feasibility of a thick target experiment.

# Chapter 1

## Introduction

### 1.1 Big-bang nucleosynthesis

Today's accepted cosmological models imply as the triggering event for the creation of our universe an expanding process called the Big-bang. The very early begin of this expansion, which arised from a singularity, is characterized by its extremely dense and hot nature, which goes beyond our understanding of physics. Main indications of this cosmological genesis are the observed expansion of the galaxies [1] and the measured microwave background at 2.7 K [2]. Although all models fail to describe the singularity, the process itself can be modeled from a point in time, which can be conceived with the current knowledge of physics. However, some fundamental properties of the early universe must be assumed.

One of these key assumptions is the baryon to photon ratio  $\eta$ , which allows to deduce  $\Omega_B$ , the baryonic density of the universe. Including  $\Omega_B$  together with the cross sections of production and destruction processes of the lightest nuclei in a framework of thermonuclear reaction rates, as discussed in [3], a primordial abundance of elements can be calculated [4] [5].

Figure 1.1 shows the predicted primordial abundance of some light elements from [5] and the comparison to astronomical observation.

Note that these calculations predict primordial abundances of D,  $^3\text{He}$ ,  $^4\text{He}$  and  $^7\text{Li}$ , which are spanning more than 10 orders of magnitude. Recently, however, the study of the Cosmic Microwave Background anisotropies from the measurements of the WMAP mission has shown a new approach to pin down  $\Omega_B h^2$ . The accepted value of  $\Omega_B h^2 = 0.0224 \pm 0.0009$  [7] sets tight constraints to models of BBN calculation.

At the time when the present experiment was proposed, the only method to put constraints on  $\eta$  (or  $\Omega_B h^2$ ) was the comparison of astronomical measurements of primordial mass fraction of elements in the interstellar medium to theoretical predictions as done in [8]. Thus, any additional primordial abundance would help to constrain  $\eta$  and the next best candidate, from the point of view of next highest predicted abundance, is  $^6\text{Li}$  as discussed in [6]. Present day  $^6\text{Li}$  is thought to be produced mostly by cosmic ray spallation in

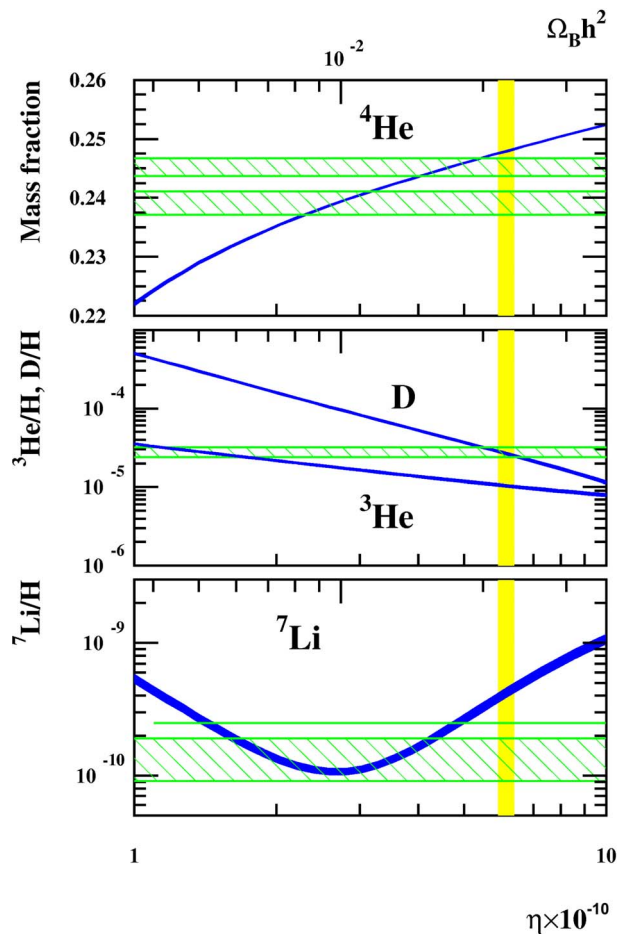


Figure 1.1: Abundances of  ${}^4\text{He}$  (mass fraction),  $\text{D}$ ,  ${}^3\text{He}$  and  ${}^7\text{Li}$  (by number relative to  $\text{H}$ ) as a function of the baryon to photon ratio  $\eta$  or the baryonic density of the universe  $\Omega_B$  ( $\Omega_B$  is here multiplied with a factor  $h^2$ , where  $h$  is the Hubble parameter expressed in units of  $100 \text{ km s}^{-1} \text{ Mpc}^{-1}$ ). The hatched green area represent the range of observed primordial abundances. The vertical yellow band represents the  $1\sigma$ -limits for  $\Omega_B h^2$  from the WMAP data [7]. This figure has been reproduced from a picture in [5].

the galaxy and hence the primordial abundance suffers from depletion and enrichment processes. The evolution of  ${}^6\text{Li}$  in standard cosmic-ray nucleosynthesis has been reviewed in [9]. However, it is possible that the levels of this isotope in hot and extreme low-metallicity halo stars could reflect its primordial abundance. This implication of primordial lithium abundances in such halo-stars is still subject to controversial discussions among the astrophysical community.

Measurements of the metallicity of  ${}^6\text{Li}$  in such stars were first reported in the beginning of the nineties by Smith et al. [10] and later by Asplund et al. [11] in 2006, where the astronomical uncertainties of the measurement have been reduced considerably. Figure 1.2 from [12] summarizes the limits from observational abundances of lithium and compares them to the BBN calcu-



lation of Coc et al. [5] and to the prediction from the WMAP evaluation. Both lithium isotopes  ${}^6,{}^7\text{Li}$  show a disagreement between observed abundance and the calculated one in combination with the WMAP limit. But for the case of  ${}^6\text{Li}$  there is a total mismatch of observation and prediction from BBN.

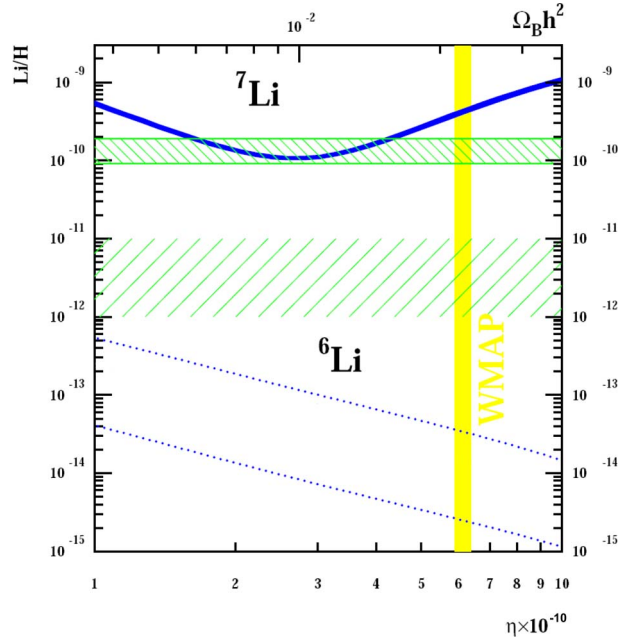


Figure 1.2:  ${}^6,{}^7\text{Li}$  abundance as a function of the baryon to photon ratio  $\eta$  or the baryonic density of the universe  $\Omega_B$ . The dashed green areas represent the range of observed  ${}^6,{}^7\text{Li}$  abundance. The solid blue line corresponds to the BBN-evaluated  ${}^7\text{Li}$  abundance and the dotted blue lines define the upper and lower limit of the BBN prediction of  ${}^6\text{Li}$ . The vertical yellow band has been deduced from the WMAP data. This figure has been reproduced from a picture in [12].

The non-triviality of the interpretation of the astronomical observation has already been pointed out, but since BBN calculations strongly depend on the precise knowledge of the cross sections of nuclear reaction rates it is worthwhile to address the focus on this issue.

### 1.1.1 Nuclear reaction network of ${}^6\text{Li}$

The model of BBN describes a complex network of nuclear reactions in a time and temperature dependent framework. The first nuclear reaction after the Big-bang, which led to significant production of deuterium occurred between protons and neutrons. This happened at a temperature corresponding to the binding energy of the deuteron of 2.2 MeV. At the time the universe was around 1 s old and its rapid expansion cooled it further down to temperatures, where other thermonuclear reactions were possible, and the next light nuclei  ${}^3\text{H}$  and  ${}^3\text{He}$  could be build up. The growing network of light



## 1.2 Theoretical and Experimental cross section data of the ${}^2\text{H}(\alpha,\gamma){}^6\text{Li}$ radiative capture reaction

While the cross section of the destruction process  ${}^6\text{Li}(p,\alpha){}^3\text{He}$  is known down to energies where the effect of electron screening matters, the producing reaction of the deuteron-alpha capture has not yet been seriously studied at BBN-relevant energies of 50 to 400 keV.

Figure 1.4 shows the present situation of the published experimental data and the cross section is plotted in terms of the astrophysical S-factor. According to [17] the cross section  $\sigma$  can be expressed as

$$\sigma(E) = S(E)\exp(-2\pi\eta)\frac{1}{E}, \quad (1.1)$$

where  $S(E)$ , defined by this equation, is referred to as the astrophysical S-factor. The quantity

$$\eta = \frac{Z_1 Z_2 e^2}{\hbar\nu} \quad (1.2)$$

is the Sommerfeld parameter,  $Z_1$  and  $Z_2$  being the charge numbers of the interacting nuclei,  $e$  is the unit of the electric charge,  $\nu$  is the relative velocity and  $\hbar$  the reduced Planck constant.

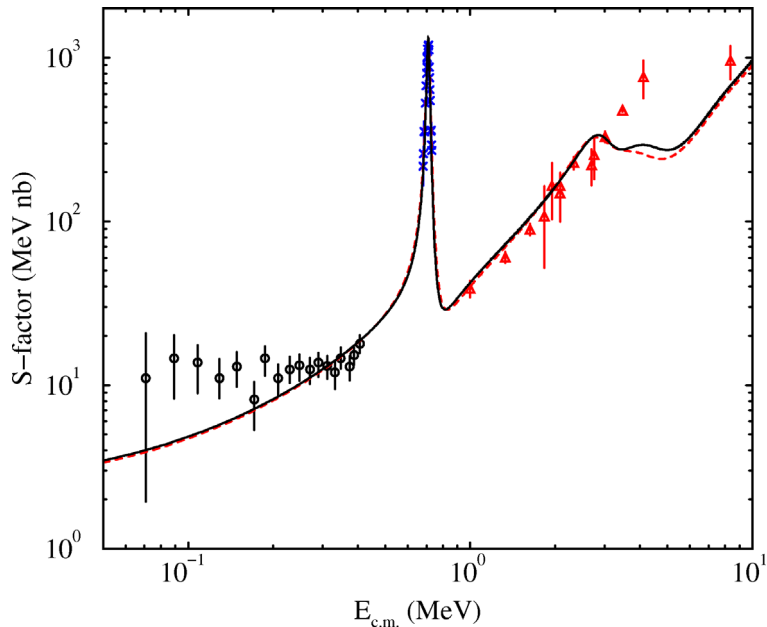


Figure 1.4: The solid and the dashed curves represent the total S-factor calculated in [13]. The data of [24] (triangles) and [25] (crosses) are direct measurements of the radiative capture. The data of the indirect measurement (circles) of [16] is derived from the graphical representation in [17].

The data points at the  $3^+$  resonance ( $E_{c.m.} = 711$  keV) and above are direct measurements of Mohr et al. [25] and Robertson et al. [24]. The data below the resonance, which cover the BBN relevant region, represents the indirect measurement of the Coulomb dissociation of  ${}^6\text{Li}$  ( ${}^{208}\text{Pb}+{}^6\text{Li}\rightarrow{}^{208}\text{Pb}+\alpha+d$ ) of Kiener et al. [16]. However, the results of Kiener et al. are affected by large systematic uncertainties and the experiment has been recently repeated at GSI by Hammache et al. [12].

Since the calculated limits of the primordial abundance of  ${}^6\text{Li}$  shown in figure 1.2 [12] are based on the data of Kiener et al., the BBN prediction of Coc et al. might change with the latest available data from Hammache et al. Nevertheless the breakup reaction of  ${}^6\text{Li}$  as a substitute for a direct measurement is not satisfactory. The analysis of the kinematics of the breakup reaction involves theoretical assumptions on the nuclear potential with respect to the contribution of the dipole moment  $E_1$  and the quadrupole moment  $E_2$ . These assumptions can be a source of large systematic errors.

### 1.2.1 Theoretical cross section

The cross section for the  ${}^2\text{H}(\alpha,\gamma){}^6\text{Li}$  process at the energies relevant for BBN has been computed by Nollett et al. by the use of variational Monte Carlo method, where the generated final state is a six-body wave function from the Argonne AV18 and Urbana IX potentials [13]. Their calculations show that the result does not depend much on the chosen potential and that the difference in the region of interest is negligible.

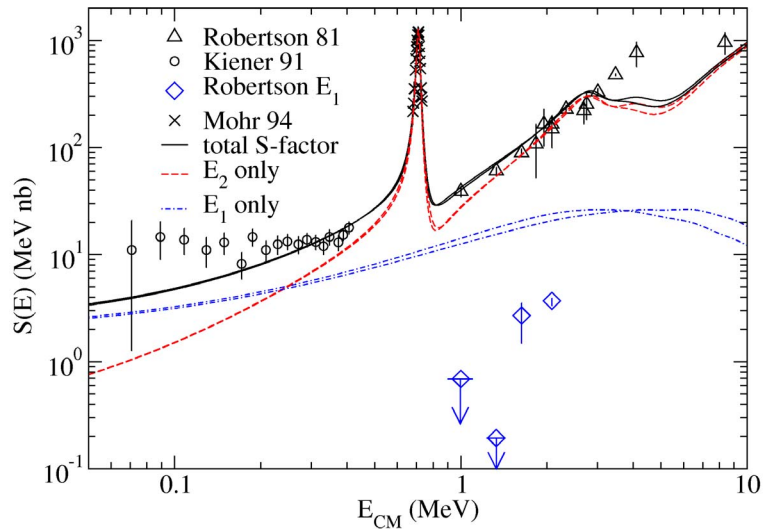


Figure 1.5: The solid lines represent the theoretical calculation of the total  $S$ -factor computed by K. M. Nollett [15]. The dashed lines show the contribution to the  $S$ -factor from  $E1$  and  $E2$ . The variation in theoretical curves are due to different choice of parametrization of the effective potential function of the Hamiltonian.

Those calculations include all initial states with  $L \leq 3$  and the M1, M2, E1, E2 and E3 operators. As described in [15] the reaction  ${}^2\text{H}(\alpha, \gamma){}^6\text{Li}$  is isoscalar, so direct E1 transitions are suppressed. The M1 transition from S-wave initial states is also suppressed. The consequence is that the reaction at energies between 0.4 and 3 MeV is dominated by the E2 contribution. At about 250 keV the isoscalar E1 is computed to be half of the total cross section. It becomes even more important at lower energies as the centrifugal barrier disfavors the E2 contributions arising from D waves. Figure 1.5 shows the result of this theoretical calculation [15]. While the theoretical curve matches well the experimental data of the total S-factor of the direct experiment, the data points of the E1 from Robertson et al. [24] cannot be reproduced at all. The authors in [15] suggest that the shortcoming may be in the data.

A representation of the S-factor in units of barn is given in figure 1.6. The prediction of the cross section at 400 keV is below 1 nb, as the reaction is suppressed by the Coulomb repulsion, the potential between the  $\alpha$  and the deuteron being 777 keV. Hence, the resulting sub-nanobarn cross section makes high demands on the experimental setup.

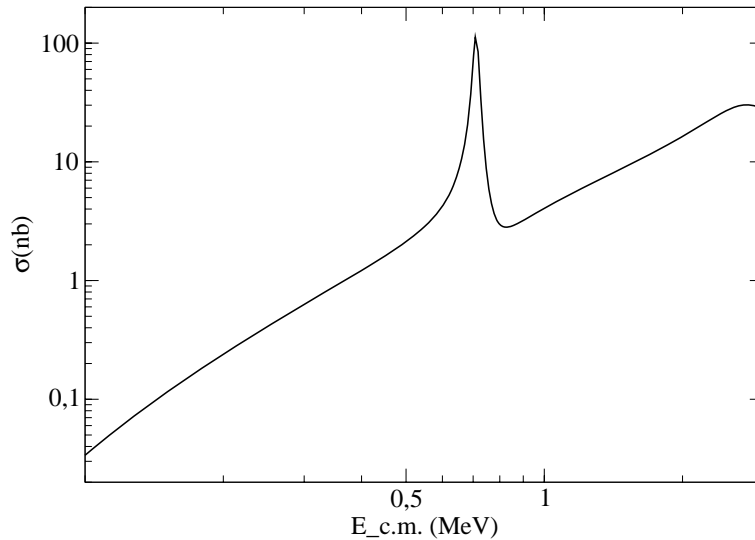


Figure 1.6: *The solid line represents the theoretical calculation of the total cross section made by K. M. Nollett [14], which can also be deduced from the S-factor calculation in [15].*

# Chapter 2

## Experiment

The description of the experimental setup has been divided into six sections for the purpose of clearness. The first two sections describe the accelerator and the beam line.

The Cockroft-Walton accelerator is only able to deliver a continuous beam. But an important requirement of the experiment is a time of flight information in order to tag an event coming from reactions in the target. Hence the  $\alpha$ -beam has been bunched by a chopper. This chopper device has been added to the beam line and will be described in a subsection.

The development of the cryogenic targets at the University of Basel and the different detectors employed are discussed in detail. The main detector, which is enclosed in a lead shielding, is presented in section 2.5.

The description and explanation of the experiment ends with the section dedicated to the data acquisition.

### 2.1 Accelerator

The Cockroft-Walton accelerator in Basel was built from 1957 to 1960 by E. Haefely & Cie and Prof. Dr. Paul Huber. It was designed to reach a maximum high voltage of 4 MV in order to accelerate ions.

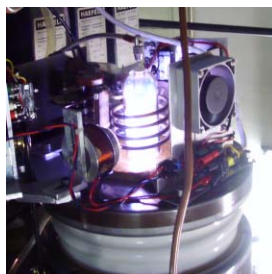


Figure 2.1: *Ion source placed on top of the white porcelain acceleration tube. The coils around the bell-shaped top produce a high frequency field, which ionize the helium gas inside the bell.*

The ions are produced from a flowing Helium gas using a high frequency irradiation. An electrode extracts then the ions downwards to the acceleration tube as shown in figure 2.1. The accelerator is equipped with 20 potential steps which can be tuned up to 200 kV per step. The voltage of 4MV can be generated using a Greinacher-style multiplier (see figure in appendix C) [18]. However, in practice only 3.5 MV could be attained.



Figure 2.2: *On the left picture one can see the high voltage cascade with the white porcelain acceleration tube and on the right the isolation tank of the accelerator.*

The whole accelerator, with the cascade of the high voltage and the ion source, is enclosed by a steel tank of around 6 m height and 2.5 m diameter as shown in figure 2.2. Because of the high tension the accelerator needs to be isolated from the environment in order to avoid an electric breakdown, the tank is filled with dry nitrogen at a pressure of 6 bar. The accelerator tube (white porcelain) is, as the following beam line, evacuated and contains special formed acceleration electrodes which are connected to the potential steps of the Greinacher-style multiplier. These pot-like electrodes center the beam and accelerate the ions downward.

## 2.2 Beam line

Once the continuous beam has passed through the accelerator into the external beam line, the optics play a key role for the quality of the beam structure. For a schematic view of the beam line, see the drawing in appendix D.

A first dipole ('Oerlikon Magnet'), which is placed under the steel tank of the accelerator, performs a rudimentary filtering of the beam and leads the  $\text{He}^{2+}$ -beam through a two quadrupole assembly, which focuses the beam into

the banana-shaped analyzer magnet. The analyzer magnet is responsible for the energy selection of the beam and bends the beam into an inclined upward direction. The beam passes again a quadrupole assembly and is then bent by two magnets into a horizontal direction. Then the horizontal beam is led through a setup of magnets and through a slit-chopper-slit arrangement, this in order to structure the beam into bunches.

The quality of the beam is checked once in a while using a remote controlled beam profile scanner. The time structure is measured via the  $\alpha$ -C elastic scattering. Therefore a thin carbon foil is inserted into the line of beam and a detector close after the foil counts the scattered  $\alpha$ -particles as a function of time. The beam is stopped in the cryogenic target or in the Faraday cup, which can be placed in front of the target once a while in order to measure the beam current.

The beam line is also equipped with turbo pumps at many locations to keep the vacuum level at  $2 \cdot 10^{-6}$  mbar. In the drawing in appendix D only some of the pumps have been mentioned. Four pumps which were located between the first quartz monitor and the Oerlikon-magnet are not shown.

Special attention has been dedicated to the very last section of the beam line inside the shielding housing, where the detector is placed. The beam line is made of OFHC copper and the last section of it through the detector is widened in diameter till physical contact with the detector, as shown in figure 2.3. This in order to offer free space for the experimental components like the target, the Faraday cup and a silicon detector in the vacuum enclosure of the beam line.

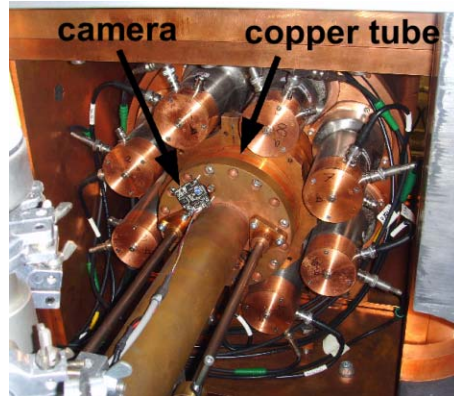


Figure 2.3: *The beam line is widened in diameter before passing through the detector. The adapter flange is equipped with a vacuum tight quartz window and a camera, which allows online monitoring of the target. The copper tube inside the detector has an outer diameter of 149 mm and is 2 mm thick.*



## 2.2.1 Beam energy selection

The accelerator delivers a beam, which has an energy spectrum of Gaussian distribution. In order to select a well defined energy with a spread around 1 keV a special magnet, called ‘Analyzer-Magnet’, is placed below the Oerlikon dipole magnet. The magnet consists of a curved iron core and two banana-shaped coils which are inserted in the iron core as shown in figure 2.4. The electromagnet bends the beam by  $102^\circ$ .

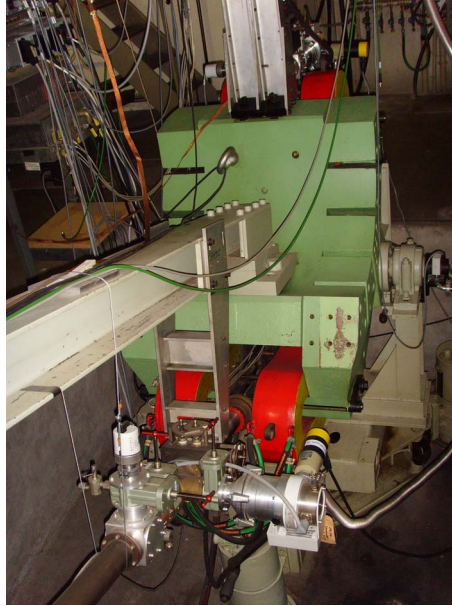


Figure 2.4: *The iron core is painted in green and the two coils are in red. The pipe of the beam line is brownish (old oxidized brass).*

The energy selection is done by keeping the magnetic field inside the magnet constant at a well defined value. The current in the coils is tuned via coupling to a proton nuclear magnetic resonance apparatus, which is located inside the magnet [19].

The energy calibration of the accelerator is performed by scanning the resonance(s) of some well known nuclear reactions e.g.  $^{27}\text{Al}(p,\gamma)^{28}\text{Si}$ . The current in the coils is tuned in such a way to attain a maximum gamma ray flux from the involved nuclear reaction. The correlation of the induced magnetic field to the response of the proton nuclear magnetic resonance-frequency pins down the exact beam energy value to a measurement of a frequency.

The calibration of Löffler in 1975 [19] has been verified by Daniel Sacker and Cedric Carasco in 2001 [20].

## 2.2.2 Beam chopper

When the  $\alpha$ -beam strikes the target, both gammas from the d- $\alpha$  capture reaction and neutrons are produced. It is mandatory to distinguish the different

source of signal in the detector from each other. This can be achieved by tagging an event with a time of flight information. To generate such a time information in the DaLi-experiment, the continuous beam of the Cockroft-Walton accelerator has to be structured into bunches.

A modification of the source was considered to be impracticable and too difficult. So a beam chopper apparatus has been built and plugged into the beam line (see the location in the drawing in appendix D). The operating mode is quite simple as sketched in figure 2.5.

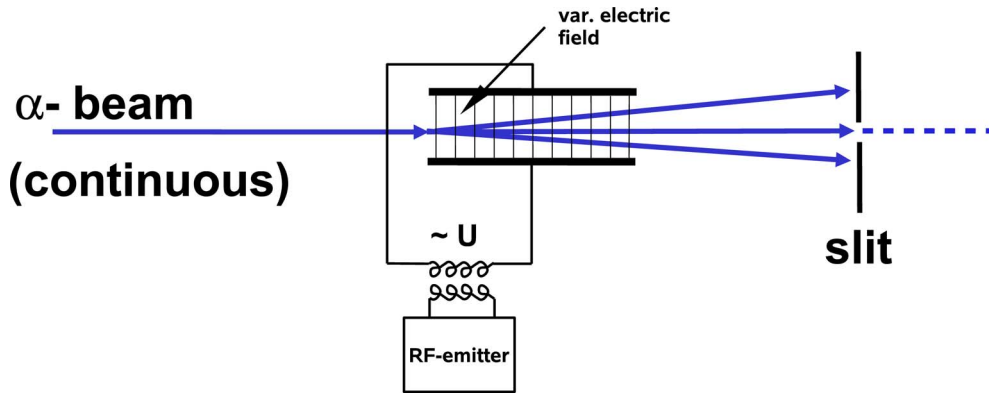


Figure 2.5: *Sketch of the beam chopper.*

The continuous single ionized beam passes in-between two parallel copper plates, which are connected to a coil. The distance of the copper plates to each other is 2 cm (see figure 2.7). A RF-emitter of 17.06 MHz and a power of maximal 200 W induces over a coil, which is placed next to the coil of the copper plates as shown in figure 2.6 (left), a high voltage of several thousand volts. Between the plates a modulated electric field deflects the beam by horizontally sweeping it. At a distance of one meter a slit cuts the beam into bunches. In correspondence to the modulation frequency the bunches are separated by 29.3 ns.

In order to avoid noise from the RF signal, the emitter has been enclosed in a Faraday cage. The cage then was grounded to the same ground of the accelerator via the metallic beam line. Figure 2.6 (right) shows the wrapped RF-emitter below the steel barrel containing the copper plates of the chopper.

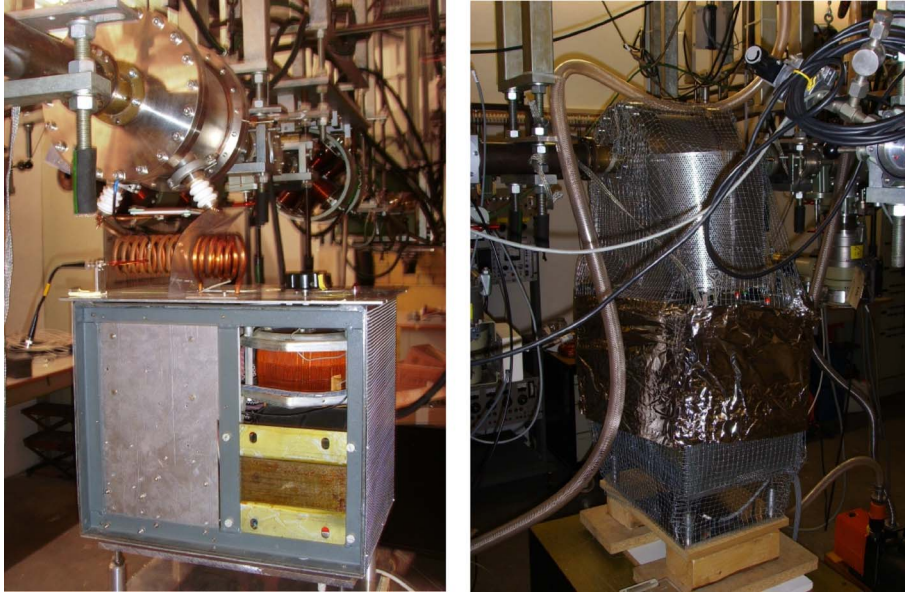


Figure 2.6: *On the left picture the RF-emitter is coupled via coils to the beam chopper. The coils are electrically isolated from each other via a PVC-sheet in order to prevent a short circuit. On the right the chopper apparatus is wrapped in a Faraday cage to prevent electromagnetic pollution.*



Figure 2.7: *Steel barrel containing the copper plates of the beam chopper. The plates are 125 mm wide (in direction of the beam), 135 mm in height and 5 mm thick. The parallel plates are electrically isolated and at distance of 2 cm.*

### **Beam profile**

In order to achieve a well defined bunch structure, the beam profile close to the 1 mm slit has to be as narrow as possible. The profile needs to be nar-

rower than the slit of one millimeter. This is done by pre-cutting the beam with a 2 mm slit before it is passing the chopper (see drawing in appendix D). The profile is monitored once a while via a beam profile monitor just before the 1 mm slit. This monitor drives horizontally a thin wire through the beam line and collects the charge of the beam. On a x-y-oscilloscope the signal can then be converted into a width. Usually the beam profile was estimated to be as narrow as 0.73 mm, which was less than the required 1.0 mm of the slit width.

In addition to the profile monitor a quartz target, which can be inserted into the beam line, allows also to have an optical view of the beam. In figure 2.8 one can see the scintillation of the quartz target due to the impact of the beam.



Figure 2.8: *The beam is hitting a quartz and through scintillation and luminescence revealing its position.*

### Time structure

In order to measure physically the time separation of the beam bunches, a setup for the measurement of elastic scattered  $\alpha$ -particles on a Carbon target was arranged. Figure 2.9 shows schematically how the setup looks like.

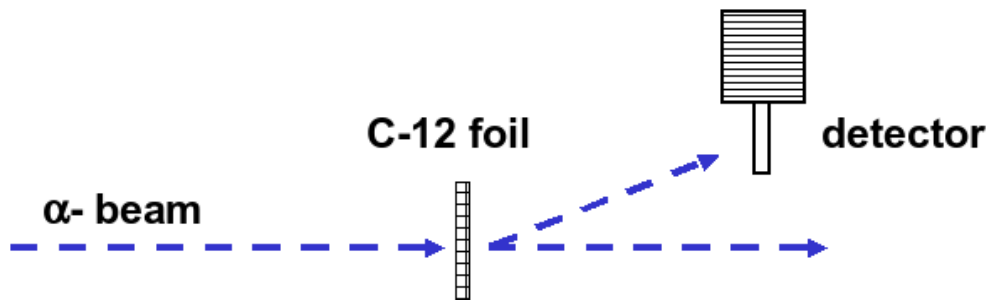


Figure 2.9: *The  $\alpha$ -beam is striking through a thin carbon foil. The elastic scattered  $\alpha$ -particles are then detected by a plastic scintillator detector.*

The elastically scattered  $\alpha$ -particles are detected by a detector. The detector consists of a thin plastic scintillator, which is coupled over a light guide to a R 1450 photomultiplier from Hamamatsu as shown in figure 2.10. The photomultiplier has an outer diameter of 19 mm (of which 15 mm diameter

is for the photocathode) and features a specially low transit time spread of 0.73 ns FWHM. The detector is covered with a pinhole (diam. 2 mm) iris in order to reduce the rate of detected particles. The plastic scintillator was placed at a distance of 140 mm from the carbon target and 33 mm off the center of the beam line. The carbon foil was mounted onto a support, which could be moved into the beam line for the measurement of the time structure. The thickness of the foil was  $10 \mu\text{g}/\text{cm}^2$ .

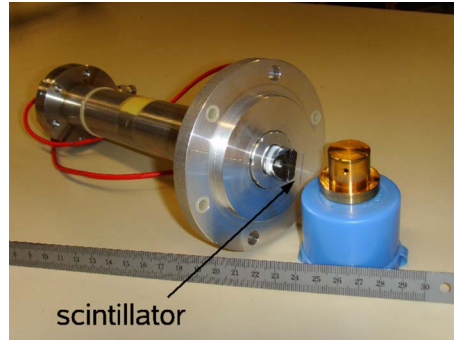


Figure 2.10: *The scintillator is 16 mm wide and has a height of 8 mm with a thickness of 0.5 mm. The pinhole iris was made of copper and coated with gold.*

The signals of the detector are brought into a coincidence logic with the RF of the chopper. The drawing E in appendix A shows the electronic setup of the logic and how the relative time of detection is measured. The time spectrum is recorded via data acquisition and can be displayed as a histogram as shown in figure 2.11.

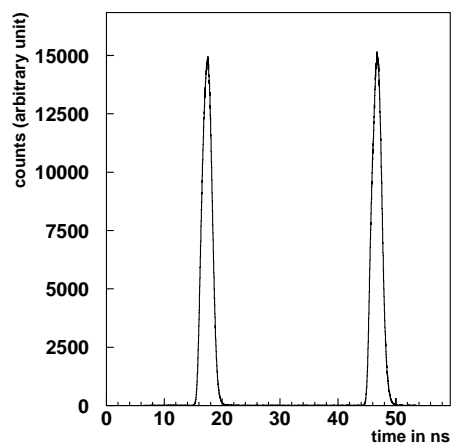


Figure 2.11: *The time structure of the beam measured via  $\alpha$ -C scattering.*

As given by the frequency of the emitter the bunches are separated 29.3 ns from each other with a spread of 1.7 ns FWHM. The evaluated spread overestimates the physical spread of the beam bunches, since this value has to be unfolded for the transit time spread of the photomultiplier, the time resolution of the scintillator and the one of the electronics. Assuming a quadratic summing rule for all contributions, the combined time resolution of the scintillator and electronics is of the order of 0.2 ns, and a physical time spread of 1.5 ns can be estimated.

The spread of the bunches does strongly depend on the beamguide and on the power of the RF-emitter. The optics of the beam line has to guide the beam precisely through the chopper and the slits in order to avoid artifacts on the beam structure. The power of the RF-emitter is a direct effect onto the deflection of the beam. Hence, the higher the power, the stronger is the electric field between the copper plates of the chopper. A high power increases the deflection of the beam and hence the time needed for the beam to pass over the slit decreases for the benefit of the time spread of the bunches. But this occurs at the cost of the beam intensity on the target.

### 2.2.3 Faraday cup

The measurement of the beam charge is performed in two ways. While one method provides an absolute measurement using a Faraday cup, is the other one a relative measurement. The relative measurement consists of a setup of irises in the beam line, which collects the charge deposition of the deflected beam after the chopper. Figure 2.12 shows the setup of the relative measurement of the beam current. How the relative measurement is implemented

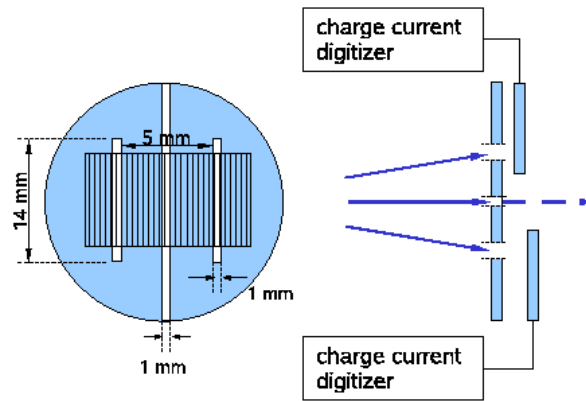


Figure 2.12: The left picture is a sketch of the front view of the slit arrangement, which is placed 1 m downstream after the chopper. The hatched area represents the swept pathway of the chopped beam. The beam sweeps over three slits. The picture on the right shows a top view. While the central slit allows the beam to reach the target, the lateral slits are closed by two electrically isolated metal plates. These plates are connected to a digital current analyzer, which allows to feed the signal into the data acquisition.

into the electronics is documented in drawing D in appendix A. The current is converted into a digital signal, where the frequency of the signal is proportional to the current. This digital signal is counted with a scaler by the data acquisition.

This method allows to monitor the current during the data taking of the experiment without affecting the beam. However, this method is not suitable for an absolute charge measurement, the recorded scaler values have to be calibrated by an absolute measurement.

In principle the absolute current measurement works the same way as for the chopper-slits assembly. The electronic setup is documented in drawing D of appendix A. But since it is an absolute measurement one has to make sure that no charge is lost. When the beam of accelerated ions is stopped on a target, some of the electrons of the induced ionization are backscattered. This charge would be lost and not measured. In order to avoid this loss the charge collector is formed as a cup, the so-called Faraday cup. In addition a ring with a counter voltage of  $-100\text{ V}$  above the cup acts as a barrier and prevents backscattered electrons to escape. Figure 2.13 shows the Faraday cup used in this experiment. The cup could be inserted directly in front of

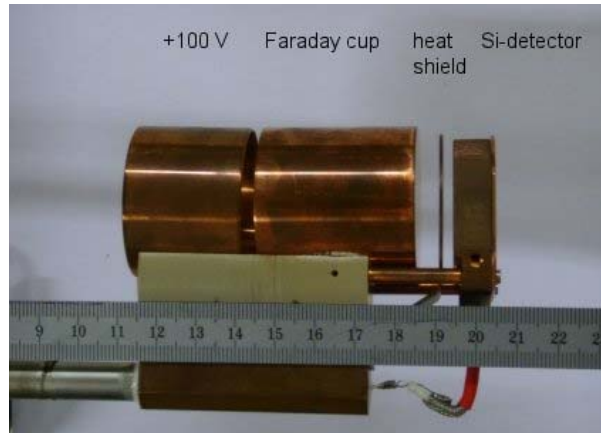


Figure 2.13: *The ring with a counter voltage and the Faraday cup are electrically isolated on a support made of ‘Peek’. A silicon diode detector is mounted behind the Faraday cup and in-between a thin copper plate shields the Si-detector from heat during the measurement of the beam current.*

the cryogenic target and during the measurement of the DaLi-reaction it was parked outside of the detector, laying on the beam pipe. The beam current measurement via Faraday cup was usually performed once a day and allows to convert the values from chopper-slits scalers into a current respectively into a charge.

Of course this type of correlation needs a calibration of the scaler value of the Faraday cup. This calibration has been performed during the commissioning by feeding well defined current values from a current generator into the signal line, which is connected to the DAQ.

## 2.3 Cryogenic targets

A good tool for background discrimination is to detect all products of the reaction. In our case these are the gamma from the capture reaction and the resulting  ${}^6\text{Li}$  nucleus. While the gamma can easily traverse matter without substantial attenuation, the  ${}^6\text{Li}$  is rapidly stopped at the location of production, if the target has a considerable density or extension and the kinetic energy of the lithium nucleus is low. To overcome this issue previous experiments of [24] and [25] made use of gas-jet targets. This method offers the possibility to detect the lithium nucleus as described in [24]. Another feature of the gas-jet target is that the beam almost passes through the target and can easily be measured by a Faraday cup [25]. Another advantage is that the measurement of the cross section occurs at a definite energy of the incident  $\alpha$ -particle. The drawback of this method is the low luminosity due to the low density of a gas-target; this makes the measurement below the resonance of c.m. 711 keV, where the cross section rapidly drops, very difficult.

A thick target, where the  $\alpha$ -beam is stopped in the target, can increase the luminosity a lot. But because helium is an inert gas and does not become solid under technical and physical reasonable conditions, there is no solid target of this kind available. So only a deuterium target is practical. Past efforts of Cecil et al. [26] used a cooled deuterated polyethylene target. But this material suffers of a carbonization process, where the beam strikes the target and hence it is difficult to guarantee a constant deuterium population. After the evaluation period in Basel for this experiment we have come to the conclusion that a cryogenic target of deuterated water and even of pure deuterium ice is the best solution for a thick target experiment for the  ${}^2\text{H}(\alpha,\gamma){}^6\text{Li}$  reaction.

The following subsections describe two setups for a cryogenic target, one for deuterated water ice and the other for solid  $\text{D}_2$ -ice. For the final data taking only the deuterated water ice target was employed, since the cryogenic expander for the refrigeration of deuterium broke during a test measurement in September 2006. Nevertheless it is worth to document this type of target, because of the success to achieve a more than 1 mm thick solid  $\text{D}_2$ -ice target.

### 2.3.1 Solid $\text{D}_2$ target

Experiments, where ultra cold neutrons sources are required, are often based on the exposure of solid deuterium to a neutron beam from a reactor. The deuterium acts as a moderator and has also the benefit of a low absorption cross section for neutrons. The luminosity of such a moderated neutron beam depends on the flux from the reactor and on the volume of the cryogenic moderator. Given a flux of neutrons from a reactor and the deposited heat load on a solid  $\text{D}_2$  target, the size of the target depends on the thermal conductivity of the ice layer, assuming a sufficient cooling. The thermal conductivity of solid  $\text{D}_2$  is reported in [27], whereas for ortho- $\text{D}_2$  the conduc-



tivity is better than for para-D<sub>2</sub>, respectively for normal deuterium. At 5 K the thermal conductivity for normal deuterium is 0.9 W·mK<sup>-1</sup> and reaches a maximum of 1.8 W·mK<sup>-1</sup> at 7.5 K, but is as much as one order of magnitude lower than for ortho-D<sub>2</sub>.

While those solid D<sub>2</sub>-target are cooled by liquid helium, in Basel we have chosen a setup involving a cryogenic helium expander.

The expander DE-210S from Advanced Research Systems (ARS) has a nominal refrigeration capacity of 0.8 W at 4.2 K and was operated in combination with a HC-8 compressor from APD cryogenics. A photograph of the expander is reproduced in figure 2.14.

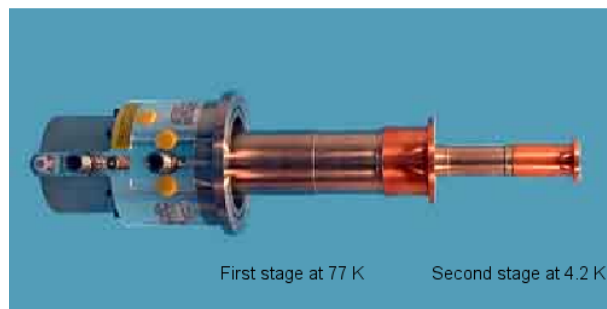


Figure 2.14: *The DE-210S expander from ARS (photograph from [www.arscryo.com](http://www.arscryo.com)) [28]. The total length is 638 mm and the diameter of the cold end is 47.2 mm. During operation a copper cylinder (not shown) shielded the second stage of the expander from the black body radiation of the environment. Therefore the cylinder was mounted on the first stage, which was cooled at 77 K.*

Several tests have been performed to determine experimentally the cooling capacity of this expander. The unmodified expander achieved a lowest temperature of 4.1 K. But for a target of the DaLi-experiment, the massive end of the unmodified expander is not suitable as a target backing, because of the attenuation of the gammas and the interaction with neutrons. Therefore a thin gas-cooled target backing has been designed and screwed on top of the second stage of the expander as shown in figure 2.15.

The target backing is made of OFHC copper for best thermal conductivity. To improve the thermal contact between the cold end and the backing, the interface is formed by a thin indium sheet. The temperature can be measured at two different points. A DT-670 diode measures the temperature directly at the second stage and a DT-470 diode is fixed on the side of the target backing at its extremity. The cap of the backing is 0.5 mm thick and the surface faced to the beam has been plated with 5 μm of gold. The inner volume is filled with 1.45 bar of Helium at 5 K. The heat load of the beam onto target is transferred by two ways. On the one hand the heat can dissipate over the cylinder of the cap directly onto the copper block with the fins and hence the heat can be absorbed by the cold end. On the other hand the helium takes the heat and transports it via convection to the fins.

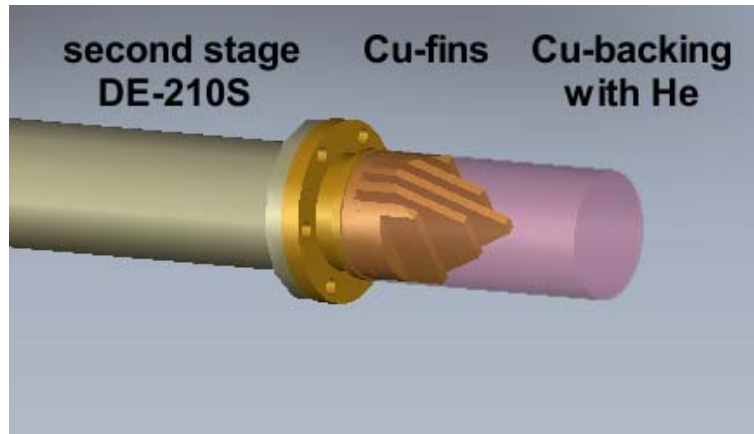


Figure 2.15: On top of the second stage of the DE-210S expander a copper block with fins for the heat exchange with the helium flow is mounted. The helium is enclosed under a cap made of OFHC copper. The closed end, which is exposed to the beam, has been plated with  $5\ \mu\text{m}$  of gold. The plated surface serves then as a backing for the ice layer. The total length of the top is 100 mm, the length of the cap is 85 mm and the diameter is 40 mm.

### Target production

The target production was performed by spraying pure  $\text{D}_2$ -gas over a sprinkler directly onto the gold plated cap, which was cooled at 5 K. Figure 2.16 shows a picture of the sprinkler, which could be placed over a vacuum tight guide at 1 cm distance from the cap. An amount of  $1850\ \text{cm}^3$   $\text{D}_2$ -gas was released over 100 minutes.



Figure 2.16: The  $\text{D}_2$ -gas sprinkler consists of a porous metal sheet, which releases the deuterium gas slowly onto the cold cap. The hollow guide is connected with a  $\text{D}_2$ -reservoir outside of the beam line.

The result was solid ice with an estimated thickness of 1 to 1.3 mm. Since the ice is clear and transparent and there was no tool to measure the effective

thickness, the given value is an estimation from calculation assuming a deposition of at least 80% and a density of  $0.2 \text{ g/cm}^3$  of the produced ice. Tests, where the cryogenic setup was mounted on a vacuum pipe, which allowed a direct view from the side as shown in figure 2.17, confirmed the assumptions. The observed ice layer was estimated to be 1 to 1.5 mm thick.

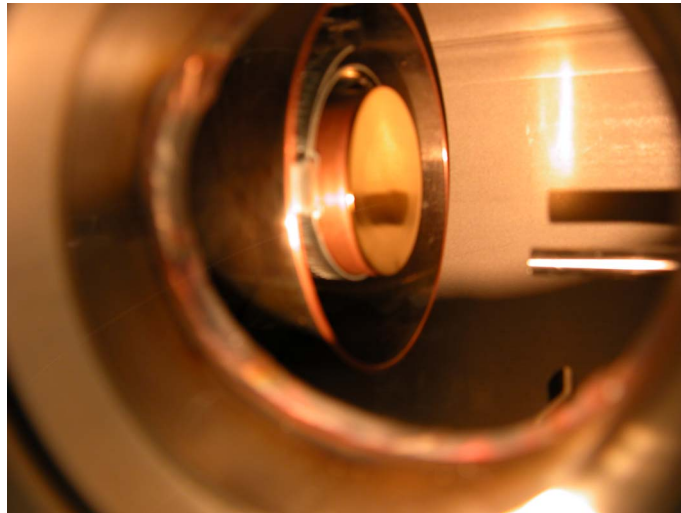


Figure 2.17: *The setup of the cryogenic target was mounted for tests into a steel vacuum tube which allowed via a glass window to view on the target. The picture shows the copper cylinder which acts as heat shield around the gold plated target backing. Around the backing a metal collar clamped a temperature diode. The small steel pipe in front of the backing was used in first tests to spray  $D_2$ -gas and was soon replaced by a sprinkler.*

## Target behavior with beam

When exposed to the  $\alpha$ -beam the target showed a faint green-blue luminescence. This is a nice feature since it allows to monitor the beam spot on the target optically.

Tests with a 1.5 MeV  $\alpha$ -beam revealed a current dependent life time of the target, which is expected, since the dissipation of the heat load is limited by the refrigeration capability of the expander and the thermal conductivity of the deuterium ice. Also the size of the beam spot has an impact on the evaporation of the ice target. A large spot has less effect on the degradation of the target. With this setup 3 to 4 cm<sup>2</sup> square sized beam spots appear to be the optimum size. A 2×2 cm<sup>2</sup> beam spot at a current of 0.1 to 0.15  $\mu$ A increased the temperature measured by the diode placed near the ice surface from 5.2 K to 5.8 K. Over 6 hours of continuous beam did not show considerable degradation. But already 0.3  $\mu$ A at 1.5 MeV heats up the target to 6.4 K and the target is evaporated within 2 hours. With the enhancement of the beam current the measured vacuum pressure rises by one order of magnitude (from  $2\cdot 10^{-6}$  to  $2\cdot 10^{-5}$  mbar), which has a negative influence on the refrigeration capability of the expander; the faint deuterium atmosphere transfers additional heat from the surrounding warm beam pipe onto the target.

It is worth to mention that the property to withstand the impact of the beam strongly depends on the way the target is produced. Different deposition rates of the deuterium gas or a different starting temperature of the backing make the degradation during exposure to the beam become faster, suggesting a crystalline structure of the ice with low thermal conductivity. During various tests of recipes for a target production, it frequently happened that the ice layer became so brittle that the beam made the layer shatter immediately. If the vibration of the target induced by the operating expander had an effect on the described occurrence could neither be determined nor excluded.

## Cryogenic D<sub>2</sub>O target

In order to perform tests of the experiment involving a less complex target as for the D<sub>2</sub>-ice, a recipe for the production of a heavy water ice target was determined. A small container with 99.99% deuterated water was therefore attached to the pipe of the sprinkler used for the deuterium gas. The water then evaporated when connected to the vacuum system of the beam tube; the flow of the vapor could be controlled using a sensitive valve and a tunable flow meter. Although the setup is not sophisticated, finding a recipe took even more time than for the deuterium gas. While water ice layers at 150 K could be easily produced at almost any deposition rate and showed no problems when exposed to the beam, the production at lower temperature <100 K revealed to be tricky. Those targets had a brittle behavior and had a high probability to shatter when the beam hit for the first time.

Nevertheless for test measurements a temperature of 150 K was sufficient to ensure condensation. Since the operation mode of the expander is continuous, the temperature of the target was kept within the range of 150 and 160 K by switching on and off the expander. This on-off mode was achieved by controlling the power supply of the expander over a switch, which was activated by the voltage of the temperature diode near the target.

### 2.3.2 Solid D<sub>2</sub>O target

As previously mentioned the expander, which allowed to operate the experiment with deuterium as well as with deuterated water, broke during a test measurement. Since the repair would have required several months and the scheduled shutdown of the accelerator was close, we opted for a new target design and the employment of deuterated water only. The expander was replaced by an insert, which put a liquid nitrogen cooled beryllium backing at the center of the detector and the same position of the gold plated copper top of the cold end of the expander.

The beryllium foil has a diameter of 38.5 mm and a thickness of 0.1 mm. The foil is circular coated (30 mm diameter) with gold as shown in figure 2.18. The coating is about 1.17  $\mu\text{m}$  thick.



Figure 2.18: *The beryllium foil with circular gold coating is cooled via liquid N<sub>2</sub>. The pipes for the nitrogen are connected to two cryogenic reservoirs. The picture was taken at the end of the experiment. The coating shows a degradation, which is due to the fact that a gold coating does not stick well on beryllium. In addition the thermal stress during the production and unfreezing of the ice targets of the measurement enhances the degradation.*

The beryllium foil is glued on a copper ring, which is cooled by the nitrogen flow as shown in figure 2.19.

The copper pipes were connected to two cryogenic reservoirs placed on the back side of the lead shielding housing; see figure 2.31. While one reservoir was filled with 100 litres of liquid nitrogen and kept at a slight overpressure, the other was almost empty and depressurized. The overpressure presses the nitrogen from the filled tank into the empty one. One load was sufficient to cool the target for around 19 hours of beam time. The target production employed the same sprinkler as for the case of the setup with the expander

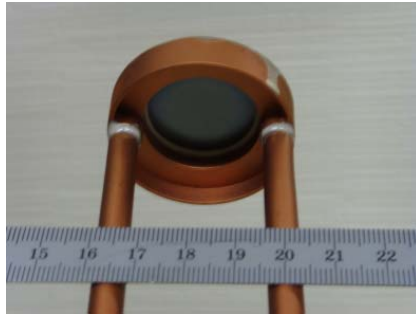


Figure 2.19: *The beryllium backing of the deuterated water ice target viewed from the back. The ring supporting the foil is part of the liquid nitrogen circuit.*

for the deposition of the deuterated water vapor.

For the ice production  $1\text{ cm}^3$  of liquid water evaporated from a little reservoir (see figure 2.20), which was connected to the sprinkler inside the vacuum system, and condensed on the cooled gold coated beryllium backing. The target was ‘renewed’ every time the liquid nitrogen reservoir was refilled. This procedure required around  $0.3$  to  $0.5\text{ cm}^3$  of deuterated water. But every 2 to 3 days the target was completely warmed up and a new ice layer was produced.

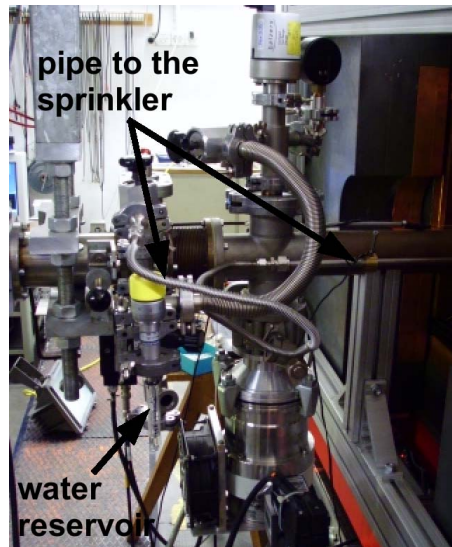


Figure 2.20: *The deuterated water is contained in a glass container. This reservoir is connected over a tunable valve to a pipe, which leads to the sprinkler of the target production.*

## 2.4 Detectors

In order to be able to detect the photon of the radiative capture of the  ${}^2\text{H}(\alpha,\gamma){}^6\text{Li}$  reaction, the experimental setup requires a detector, which fea-

tures a high detection efficiency. A good energy and time response, which is crucial for the separation of the events of the investigated reaction from background, has to be also an intrinsic characteristic of this detector. Since the experiment relies on a thickness of the deuterated target, which stops the beam within its ice-layer, one has to guarantee that this thickness is provided at any time when the target is exposed to the beam. This is ensured by measuring the backscattered alphas from the target with a semiconductor charged particle detector.

### 2.4.1 Cylindrical NaI(Tl) detector

The cylindrical shaped detector of the DaLi-experiment, which measures the photons of the investigated reaction, is a sodium iodide crystal divided into eight optically isolated segments. The cylinder is hollow and centered with respect to the target. It is placed around the beam line inside a lead-copper shielding housing. The crystal has an outer diameter of 315 mm, an inner diameter of 152 mm and a length of 340 mm.

The sodium iodide has been doped with thallium during its fabrication in order to enhance the energy resolution property of the crystal. Given its response to electrons (and hence also to gamma rays via the photo effect and compton scattering) in a scintillation process with a wavelength of maximum emission at 415 nm, the crystal well matches the spectral sensitivity of most bi-alkali photomultipliers as referenced in [21]. Figure 2.21 shows the detector placed in the shielding box.

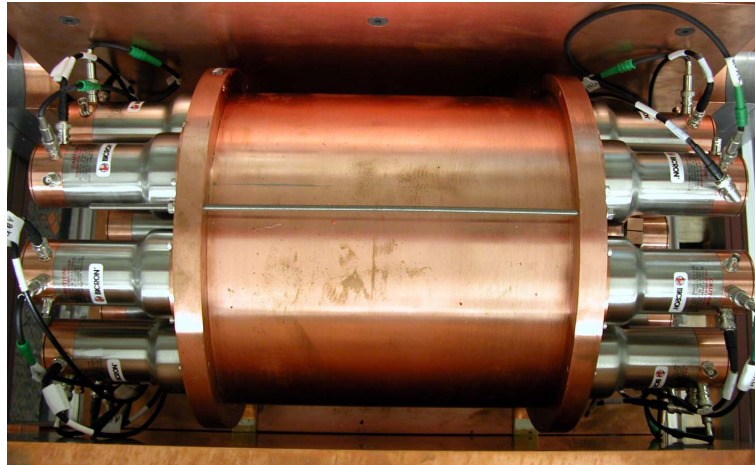


Figure 2.21: *The sodium iodide crystals of the DaLi-detector are packed in a OFHC copper casing. The signal of each crystal is read out by two photomultipliers, which are placed at both ends of a crystal.*

The present detector has been manufactured by Saint-Gobain Crystals using low radioactivity materials. The segments of crystal have been made out of one single block of sodium iodide. Special attention has been given to

the suppression of potassium, because of the naturally occurring radioactive  $^{40}\text{K}$  isotope, which has a prominent gamma ray line at 1460 keV. This has been done by choosing pure raw materials; for metal components, as for the casing, high purity OFHC copper was employed. The thickness of the casing at the inner part of the cylinder is only 0.8 mm. A thicker casing would make the gamma rays from the target suffer more of attenuation. The whole copper container has a clear acrylic finish, which electrically isolates the detector, when in physical contact with other components of the experiment, such as the beam line. The 3 inches photomultipliers R6233mod have been manufactured by Hamamatsu and are optically connected to crystal via a quartz window of 0.375 inch thickness. The phototube is wired for negative voltage operation. Tests have shown that the indicated operational high voltage of -1000 V offers indeed the best signal to noise ratio for this tube.

### Energy resolution

As mentioned each crystal is equipped with two photomultipliers, which read out the signal. The labelling of the phototubes is shown in figure 2.22. The suffix 'a' stands for the photomultiplier on the side of the target insert and 'b' refers the photomultiplier at the other end, where the beam enters into the detector.

View from cryo-side

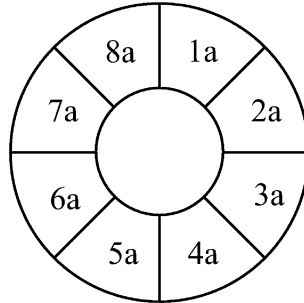


Figure 2.22: The photo-tubes are labeled clockwise from 1 to 8. The suffix 'a' refers to those photomultipliers on the side of the target insert.

The energy resolution of the crystals of the detector has been determined by measuring the emitted gamma rays of a Y-88 source, which was placed in the middle of the detector. Figure 2.23 shows the recorded energy spectrum of crystal No.2. The spectrum has been corrected for the contribution of natural background.

In order to evaluate the energy resolution, the FWHM of a Gaussian curve has been derived via a fit using a least-squared method algorithm of paw++ from CERN. In addition to the Gaussian function an exponential



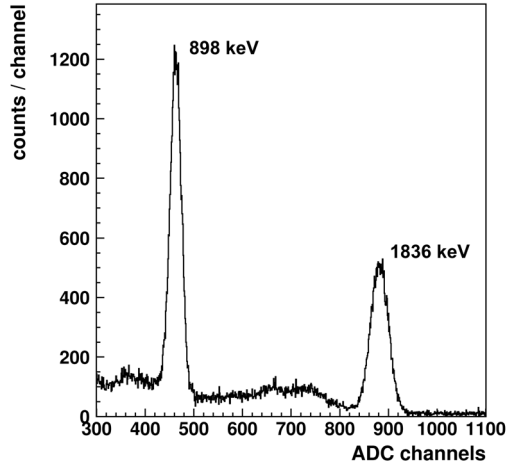


Figure 2.23: *Energy spectrum of Crystal No.2 with a Y-88 gamma ray source.*

function was added to the fit function.

$$F(x) = p_1 \cdot e^{-0.5\left(\frac{x-p_2}{p_3}\right)^2} + e^{p_4+p_5 \cdot x} \quad (2.1)$$

Figure 2.24 shows the result of the fit for the same spectrum as in figure 2.23. The resolution is then given by

$$\sigma = \frac{p_3 \cdot 2.35}{p_2 - a} \quad (2.2)$$

where  $a$  is the position of the pedestal of the ADC. So the fitted position of the peak given by the parameter  $p_2$  is corrected by the offset of the electronics.

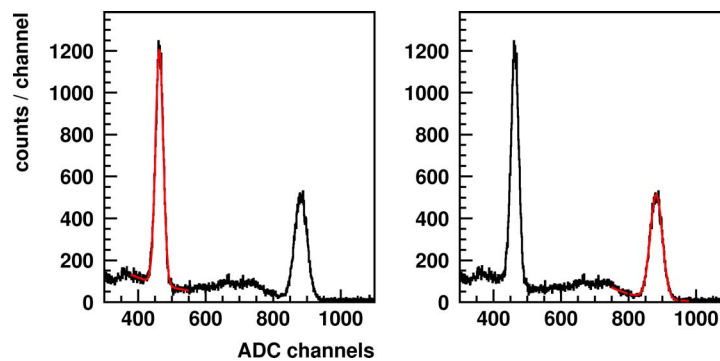


Figure 2.24: *Fitting curves in red of the Y-88 spectrum.*

The results of the measurement of the relative energy resolution for all eight crystals are shown in table 2.1. As one can see the performance of the crystals is not the same, so e.g. the relative energy resolution for crystal No.6 is 1% point better than for crystal no.1. This is not due to the quality

of the detector, but rather to the influence of the RF of the beam chopper. The powerful RF-emitter affects those channels of the electronics, which are not properly shielded from the electromagnetic pollution. This results in a deterioration of the signal-to-noise ratio and hence the energy resolution.

Crystal No.	$\sigma$ in % @898 keV	$\sigma$ in % @1836 keV
1	$7.36 \pm 0.05$	$5.98 \pm 0.04$
2	$6.57 \pm 0.04$	$5.10 \pm 0.03$
3	$6.58 \pm 0.04$	$4.96 \pm 0.03$
4	$6.82 \pm 0.04$	$5.33 \pm 0.03$
5	$7.18 \pm 0.04$	$5.84 \pm 0.04$
6	$6.31 \pm 0.04$	$4.80 \pm 0.03$
7	$6.69 \pm 0.04$	$5.08 \pm 0.03$
8	$6.89 \pm 0.04$	$5.71 \pm 0.04$

Table 2.1: *Energy resolution and estimated statistical error of the fit.*

### Efficiency measurement

The activity of the Y-88 source used for the energy calibration has been calibrated by the ‘Deutscher Kalibrierdienst DKD’. The activity on 1st November 2005 was 1.11 kBq and the relative  $1\sigma$  error of the measurement is given as 1.5%.

In order to determine the efficiency of the detector the source has been placed at the center inside the detector and the spectrum of the yttrium-88 was measured. Two types of measurement were performed:

1. The source was suspended in the center and held, longitudinally with respect to direction of the beam line, by a thin metal wire, thus, avoiding absorbers between source and detector. The target holder with the beryllium foil was therefore removed.
2. In the second measurement the source was placed on the target holder.

The flux of emitted gammas from the source can be calculated as follows

$$\Sigma\gamma_{Y-88} = A_k \cdot t \cdot B_r (1 - D_t), \quad (2.3)$$

where  $A_k$  is the activity of the source at the time of the measurement,  $t$  is the acquisition time,  $B_r$  is the branching ratio of the specific gamma energy and the term  $(1-D_t)$  refers to the dead time correction of the DAQ.

The amount of gammas in the photo-peak of the recorded spectrum, for a given interval  $[a,b]$ , can be evaluated via the fit function given in equation

2.1. The interval [a,b] spans a range, which covers up to  $\pm 3\sigma$  around the position of the maximum of the peak. The quantity  $N_a^b$  is defined by the counted events in the spectrum in the interval [a,b].

The fit function in 2.1, which constitutes of a background term (exponential function) and a photo-peak term (Gaussian peak), can then be used to derive the integral for a region of interest [a,b]. From the background term its contribution to the count rate can be evaluated via the integral

$$F_B = e^{p_4+p_5 \cdot x} \rightarrow A_B = \int_a^b F_B, \quad (2.4)$$

as  $A_B$  is the area in the interval [a,b]. The area  $A_P$  and  $\tilde{A}_P$  covered by the Gaussian function represents the measured gammas in the photo-peak. While  $A_P$  covers the area in the interval [a,b],  $\tilde{A}_P$  evaluating the integral of the Gaussian curve from  $-\infty$  to  $+\infty$ .

$$F_P = p_1 \cdot e^{-0.5\left(\frac{x-p_2}{p_3}\right)^2} \rightarrow A_P = \int_a^b F_P \text{ and } \tilde{A}_P = \int_{-\infty}^{+\infty} p_1 p_3 \sqrt{2\pi}, \quad (2.5)$$

The total fitted events of the photo-peak  $N_{Tot}$  is then evaluated as follows

$$N_{Tot} = \frac{N_a^b}{A_P + A_B} \tilde{A}_P. \quad (2.6)$$

And the efficiency  $\epsilon_{tot}$  of the detector is then defined by

$$\epsilon_{tot} = \frac{N_{Tot}}{\Sigma \gamma_{Y-88}} \quad (2.7)$$

as the ratio of the measured gamma events in the photo-peak and the estimated photons of the radioactive decay. The error of 2.7 can be evaluated via the Gaussian error propagation by the following equation

$$\frac{\delta \epsilon_{tot}}{|\epsilon_{tot}|} = \sqrt{\left(\frac{\delta N_a^b}{N_a^b}\right)^2 + \left(\frac{\sqrt{\delta A_P^2 + \delta A_B^2}}{A_P + A_B}\right)^2 + \left(\frac{\delta \tilde{A}_P}{\tilde{A}_P}\right)^2 + \delta A_k^2}, \quad (2.8)$$

whereas the term  $\delta$  represents the estimated or the statistical error of the denoted quantity. The error of the measured time, of the branching ratio and of the dead time have been neglected. Table 2.2 summarizes the results of the efficiency measurements. A comparison of the experimental results of the efficiency measurement with the results of a Monte Carlo simulation is discussed in chapter 3.4.

Gamma energy [keV]	$\epsilon_{tot}$ with target in %	$\epsilon_{tot}$ empty in %
898	$28.94 \pm 0.44$	$30.30 \pm 0.42$
1836	$19.22 \pm 0.30$	$19.75 \pm 0.30$

Table 2.2: The evaluated photo-peak efficiency of the DaLi detector is given at the two prominent energies of the gamma decay of the  $^{88}\text{Y}$  isotope. The suffix ‘target’ denotes the case, where the source has been placed onto the target holder. The measurement without any material inside the beam line is denoted by the suffix ‘empty’.

### Time resolution

In order to check the proper working of the electronics in respect of the time-of-flight processing, gamma rays from the target, which are correlated to the beam bunches, are needed. And this with a high yield. Neither the d-alpha capture nor any other background reaction e.g. the alpha-oxygen capture offer a sufficient yield of photons.

Therefore a setup for a new type of reaction was installed to overcome

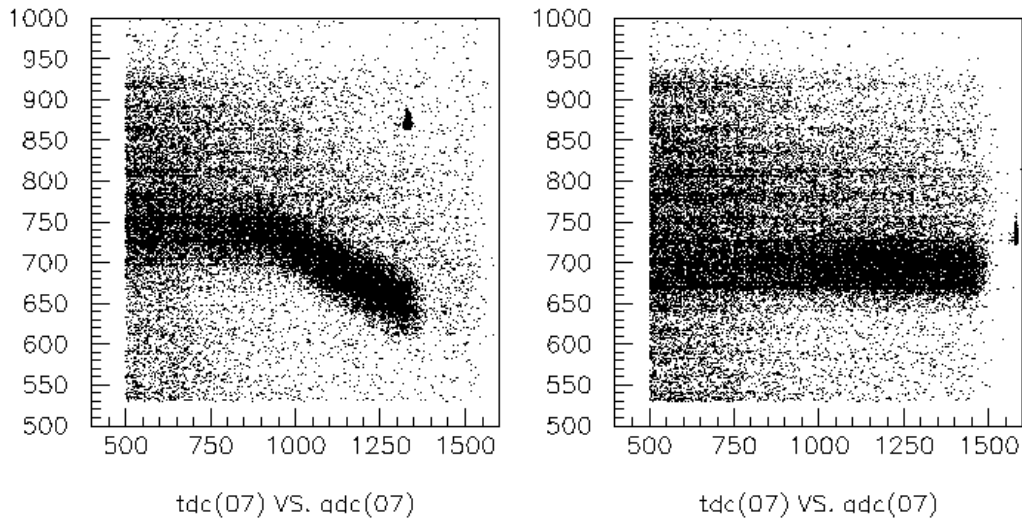


Figure 2.25: TDC vs. ADC spectra of the gammas of the  $\alpha$ -t capture. The time of arrival of the gammas should be independent of the energy. Since the constant fraction discriminator was not right adjusted, the spectrum on the left shows a walk effect. Events of higher energy trigger the electronics earlier than lower energy ones. The same channel is plotted again on the right after having fixed the electronics (also some changes to the high voltage, delays and thresholds were applied).

this issue. The reaction  $^3\text{H}(\alpha, \gamma)^7\text{Li}$  is particularly suitable. A copper sheet doped with tritium was placed at the center of the detector fixed on the copper backing of the expander. The plate was then exposed to the  $\alpha$ -beam.

The high yield of photons allows to plot online a two-dimensional spectrum of time versus energy and so check the electronics. Figure 2.25 shows a TDC vs. ADC spectrum, where the constant fraction discriminator was not well adjusted, leading to a walk effect.

Once the electronic setup was fine tuned the combined time resolution of detector and electronics could be measured. Figure 2.26 shows the time spectrum of one sodium iodide crystal. The prominent peak is due to the

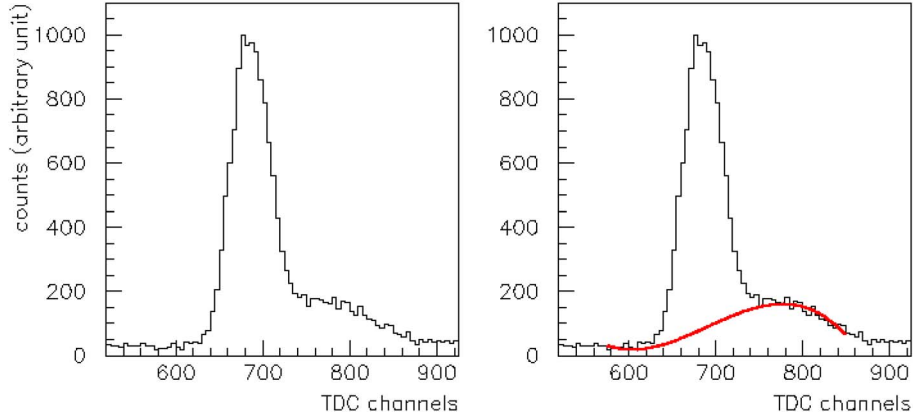


Figure 2.26: *TDC channel spectrum of crystal No.1. The background bump was approximated with a polynomial of third degree for further analysis.*

gammas, which are produced in the alpha-tritium capture. The bump on the right side is due to gammas coming from interaction of neutrons with the copper support.

In order to analyze the gamma peak, the background was first approximated

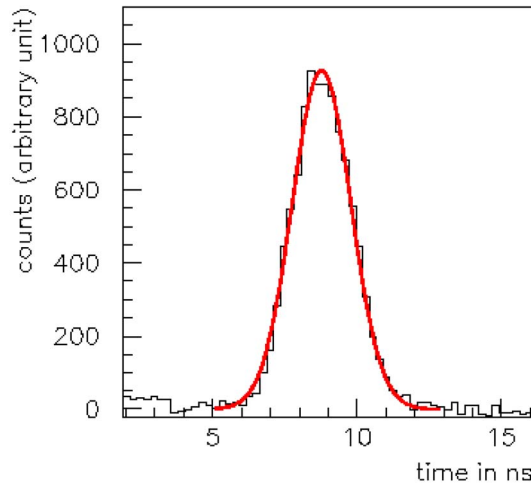


Figure 2.27: *TDC time spectrum of crystal No.1. The fit results in a time resolution of the DaLi setup of 2.42 ns FWHM.*

with a third degree polynomial. Then the approximated background was subtracted from the spectrum and the remaining gamma peak was fitted by

taking a Gaussian function plus a constant value. The result of the fit is shown in figure 2.27.

## 2.4.2 Silicon diode detector

The present experiment requires a target thickness, which stops the beam within its cryogenic layer. Knowing the maximum range of  $\alpha$ -particles through matter, either water ice or deuterium ice, one can set a minimal ice thickness to meet the experimental requirement. For  $\alpha$ -particles of 2.3 MeV the maximum range in normal water ice is  $14.5 \mu\text{m}$  and in deuterium ice  $22.5 \mu\text{m}$ . Therefore one has either to provide a direct measurement of the target thickness or ensure via an indirect measurement that the ice layer is sufficiently thick. The measurement of back-scattered  $\alpha$ -particles from the target is such an indirect measurement.

The  $\alpha$ -particles of the beam mostly undergo elastic scattering with the nuclei in the target. Their detection is provided by a full depleted silicon detector, which is mounted behind the Faraday cup (see figure 2.13) and facing the target at a backward angle of around 175 degrees. Figure 2.28 shows the silicon detector from the front. During the experiment the detector was covered by an iris with a pinhole of 1 mm diameter, so that only a small fraction of the total active area of  $300 \text{ mm}^2$  is used. The bias voltage is +70 V, the warranted resolution of 5486 keV alphas of a  $^{241}\text{Am}$  source is given as 17 keV and the nominal depletion depth is  $500 \mu\text{m}$ .

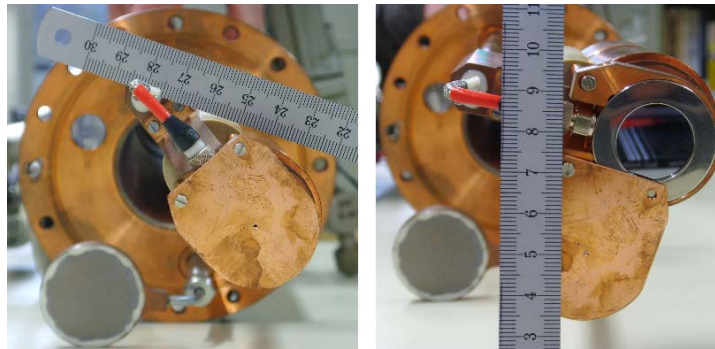


Figure 2.28: *On the left picture the pinhole iris covers the silicon detector, which is mounted behind the Faraday cup. The picture on the right shows the detector in its case.*

The electronic setup of the acquisition of the backscattered alphas is shown in the schematic drawing C of appendix A.

The described setup is intended as an online monitor of the target irradiation. A kinematic calculation of the  $\alpha$ - $^{16}\text{O}$  scattering process shows that even with a kinetic energy of the alphas of e.g 1.0 MeV, the backscattered particles still have at 170 degrees a kinetic energy of 360 keV, which makes the detection

with a standard silicon detector possible. The response of the detector to the alpha particles has been studied during tests, where the target cooling has been deliberately switched off and so allowing the beam to melt down the ice layer and reach the gold coating of the beryllium backing. Meanwhile the silicon detector recorded the events from the backscattered  $\alpha$ -particles. Figure 2.29 shows the ADC spectrum of the silicon detector during this test.

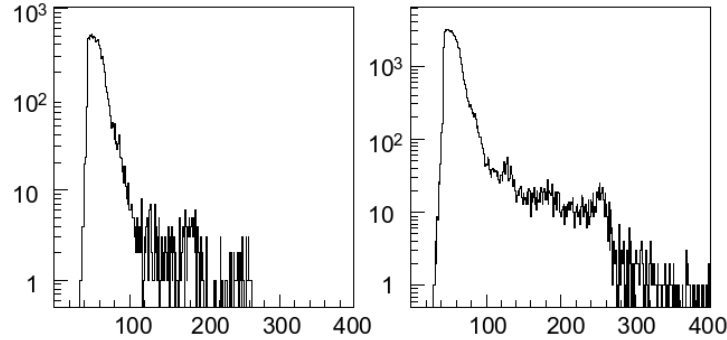


Figure 2.29: *The ADC spectra of the silicon detector. The spectrum on the left shows the detection of  $\alpha$ -particles backscattered from the oxygen in the target. The spectrum on the right shows an enhanced peak at the lower region of the spectrum (backscattered  $\alpha$ -particles from oxygen) and a broad structure from channel 140 to 160, which comes from the  $\alpha$ -scattering on gold. The broadness of this structure is due to the fact that part of the beam had to go through a residual thin ice layer before scattering on the gold surface. Hence, the detected  $\alpha$ -particles suffered from additional energy loss.*

The energy of the beam was 1.5 MeV and the current 2.13  $\mu\text{A}$ . The spectrum on the left shows the recorded events of the first minute of this irradiation test before closing the cooling of the liquid nitrogen. The spectrum on the right was recorded 22 minutes later and for 1 minute as well. The distinct broad structure from channel 140 to 260 shows that the ice layer has been melted. The kinetic energy of backscattered alphas on gold for 1.5 MeV incident energy is 922 keV. The detection of this maximum backscattering energy is seen in the small peak at channel 260.

This method has one major problem. The observation of the backscattered alphas from gold means that the ice layer has already been too thin for an unknown exposure time.

Extended tests with deuterated water ice and direct optical viewing on the target showed that providing sufficient cooling it was virtually impossible to melt down a 1 mm thick target, even within days of exposure to the beam. In order to avoid the possibility of taking data with a too low target thickness, the ice layer was renewed once a day during the experiment.

The case for the deuterium ice could not be studied as long as for the deuterated water, since the cryogenic expander broke during those tests. Although there were no backscattered alphas from oxygen, the detection of the alphas

backscattering on the gold plated backing worked as for the case with the deuterated water on the gold coated beryllium backing.

### 2.4.3 Cosmic rays detector

When primary cosmic ray particles (about 90% protons, 9%  $\alpha$  and 1% heavier particles) hit the earth atmosphere, they generate a variety of elementary particles. According to [23] at sea level, the relative intensity of charged pions:protons:electrons:neutrons:muons is about 1:13:340:480:1420. Cosmic rays in the lower part of the atmosphere are mainly muons and the total flux from above is about  $130 \text{ m}^{-2}\text{s}^{-1}$  (crossing a horizontal area) to  $170 \text{ m}^{-2}\text{s}^{-1}$  (crossing a sphere of unit cross-sectional area) at sea level [22]. For the upper half of the DaLi-detector (crystal-segments 1, 2, 7 and 8) we measured the rate of cosmic rays to be  $895 \text{ counts}\cdot\text{min}^{-1}$  which is in good agreement with an estimated rate for the DaLi-detector of  $964 \text{ counts}\cdot\text{min}^{-1}$  with the values from [22]. (The flux through a cylindrical shape has been estimated to be about  $150 \text{ m}^{-2}\text{s}^{-1}$  and then assuming the flux of muons to pass through a horizontal area equivalent to the base area of the DaLi-detector).

In order to suppress this contribution to the background, a cosmic ray detector has been placed on top and below the housing of the DaLi-detector. The detector, which was placed under the housing, consisted of 5 plastic scintillator paddles and each paddle was read out by a photomultiplier. The dimension of four paddles were each  $120 \times 500 \text{ mm}^2$  and one paddle was  $100 \times 500 \text{ mm}^2$  for a total active surface of  $2900 \text{ cm}^2$ . The thickness of the paddles was 5 mm. The placement of the paddles was such to be aligned and centered to the DaLi-detector above. In picture 2.30 one can see the paddles, which are mounted under shielding. The signal from a paddle first passes through a constant fraction discriminator and is then grouped with the other four paddles in a logic fan as described in the schematic drawing A in appendix A.



Figure 2.30: *Paddles of the cosmic rays detector under the shielding housing. The beam is coming from left.*



The cosmic ray detector on top of the shielding consists of six plastic scintillator bars  $300 \times 170 \times 170 \text{ mm}^3$  (length  $\times$  width  $\times$  height) each. The plastic bars are read out by a 5" photomultiplier. The total surface of  $3060 \text{ cm}^2$  is centered, but the longer side of 60 cm length of the rectangular surface lays perpendicular to the cylindrical shape of the Dali-detector as shown in picture 2.31.



Figure 2.31: *Bars of the cosmic rays detector placed on top of the shielding housing. The bars were additionally covered with black paper and draperies to prevent any infiltration of light into the scintillators, since the original cover was holey.*

## 2.5 Shielding

The technique of shielding is still a topic of active research. Especially for rare-event experiments, where the background due to environmental radioactivity is drowning the signal of interest by many order of magnitude, a careful design and choice of the experimental site is fundamental. Even contamination of the apparatus and shielding is, together with the contribution from cosmic rays, a challenging issue for low-level counting experiments [23]. Although the background of the DaLi experiment is predominantly caused by neutrons from a secondary reaction in the target, it is suitable to reduce the background from naturally occurring radionuclides as much as reasonably achievable.

A background investigation in the experimental hall (see figure 2.32) showed that already 10 cm of lead brings the measured activity down to a level, where intrinsic contamination of the setup and the contribution of cosmic ray become the predominant factor.

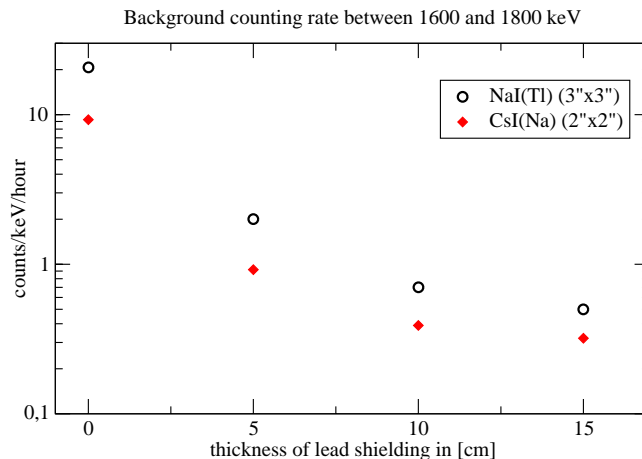


Figure 2.32: *Measured activity of background in the 4MV experimental hall. The integrated count rate between 1600 and 1800 keV is plotted as a function of the lead shielding thickness.*

Further experimental investigation with the sandwich technique of lead-copper shielding as described in [23] concluded that a shielding with 10 cm of lead and 5 cm of copper is the optimum from the point of view of background level and costs. Finally a custom made shielding was built by JL Goslar using low background lead from Boliden and OFE-copper. In appendix B the technical drawings show the details of the shield housing. The walls, roof, bottom plate and doors have a thickness of 10 cm of lead and 5 cm of copper (the copper shielding is made of a combination of a 2 cm and a 3 cm thick plate). The inner volume of the housing is  $750 \times 400 \times 400 \text{ mm}^3$  (length  $\times$  width  $\times$  height). A photograph is reproduced in 2.33.



Figure 2.33: *Shielding housing on the stand without detector, roof and doors. View from the back.*

## 2.6 Electronic setup & Signal processing

This section provides a description of the electronic setup. A detailed illustration of each step of the signal processing is documented via oscilloscope screenshots in appendix A.

The electronic setup of the experiment has been designed to respond to two major requirements. One is that the signal processing through the electronics should not affect the energy resolution and second the time resolution has to match maximum benchmarks reported in other comparable experiments or literature.

Drawing A in appendix A shows a schematic representation of the setup for the processing of the signals arriving from the DaLi detector.

The two analog signals from the photomultipliers of one crystal are first combined in a linear fan. One output of this fan passes a passive splitter for attenuation purposes and goes over a long cable delay directly into the ADC. The signal of a second output of the fan is amplified and split. This signal has to pass a first discrimination logic. While a discriminator, set to a low threshold ranging from -100 to -370 mV, performs a discrimination for low energy events, another discriminator, set to a threshold -1.0 V, blocks signals of high energies. The following coincidence of these discriminator outputs generates a logical signal only when the size of the signal is within those values.

The generated logical signal is then used to trigger the logic for further signal

processing and to open gates for triggering the TDC and ADC modules of the DAQ, but only if it is in coincidence with the RF of the beam chopper. This signal also prevents, once a signal has been accepted from the two discriminators, the whole logic to trigger again for the period of  $2.18 \mu\text{s}$  by acting as a veto on the discriminator with the low threshold. This increases the deadtime, but allows to suppress the additional triggering from compton scattered events.

Detector signals induced by cosmic rays are mainly due to muons. When these charged particles hit the detector the generated events are automatically blocked by the higher threshold discriminator. For the case that the muon hits the shielding and not the detector it may produce a shower of particles, which can pass the discrimination logic. In order to reduce this effect of background, the coincidence signal of the upper and lower cosmic rays detector is used to prevent the electronics to process an event. This is done by feeding the coincidence signal as a common inhibit gate into the coincidence unit, which is processing the RF with the signal of the photomultiplier.

### 2.6.1 RF-signal via pickup coil

Since most of the events from the detector are correlated to the bunches of the beam, the RF of the generator of the beam chopper is suited for a time information. In the vicinity of the coupling coils of the RF-generator and the beam chopper, a small one loop copper coil picks up the RF-signal for the processing in the main electronics (see schematic drawing C in appendix A). This signal is also used when measuring the time structure of the beam via  $\alpha$ -carbon elastic scattering (see schematic drawing E in appendix A). The following figure 2.34 shows the one-loop pickup coil; the thick coil of the RF-generator on the right is next of the coil of the beam chopper on the left. The thickness of the wire of the pickup coil is 2.3 mm and the outer diameter 65 mm.

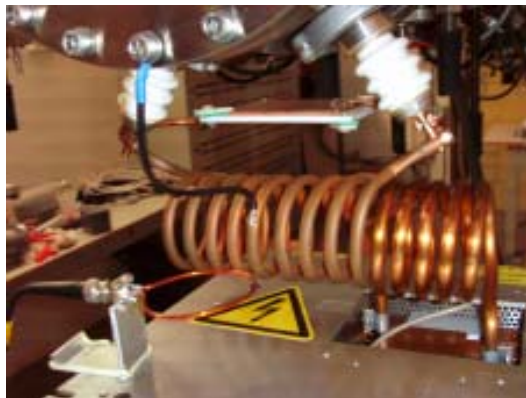


Figure 2.34: *Pickup coil and RF-beam chopper coils*

## 2.6.2 Data acquisition

The processed data from the CAMAC modules are transferred through a front-end based VCC2118 crate controller running under VxWorks to a Unix computer. The data are first stored as raw data and in a second step converted manually into paw++ hbook files. The data acquisition software called ‘Calvin&Hobbes’ has been developed in the nineties by Markus Mühlbauer and Tom Case in Basel. The software features via GUI realtime monitoring of the experiment, like current and rate monitor, and in combination with the statistical and mathematical analysis software paw++ from CERN, it allows to check online spectra of TDCs, ADCs and scalers.

In one hour of data taking typically, 80 MBytes of data were recorded. The event rate ranged from 400 Hz for the runs at 2300 keV down to 120 Hz for 1000 keV. One should note that the threshold of the discriminator for the 1000 keV runs was set to a lower value than those for the higher energies, since the background due to neutrons is the smaller the lower the incident beam energy. Table 2.3 summarizes the acquired experimental data. In addition to the pure data taking listed in the table, measurements for the current calibration were performed once per day. During the change of the beam energy, long background measurements of about 24 hours were also taken. The data acquisition itself revealed to be very stable over the whole experiment.

Beam energy in [keV]	Target	Acquisition time in [h]	Collected charge in [C]
1000	h2o	100	0.344
1000	d2o	700	2.484
1500	h2o	~40	~0.3
1500	d2o	300	2.259
1900	d2o	177	0.450
2300	d2o	120	0.213

Table 2.3: *Beam time accounting*

# Chapter 3

## Data analysis

### 3.1 Beam charge

A very important issue in order to calculate the cross section of the investigated  ${}^2\text{H}(\alpha,\gamma){}^6\text{Li}$  reaction is the knowledge of the luminosity. As described in section 2.2.3 the accounting of the beam charge relies on three steps:

- on the absolute calibration of the Faraday cup (FC),
- on regular measurement of the charge with the FC during the experiment,
- and on the subsequent calibration of the scaler events from the collected charge of the iris setup, which is placed after the beam chopper.

A graphical representation of the setup is given in appendix A in drawing D.

#### Absolute calibration of the Faraday cup

Figure 3.1 shows the schematic setup of the absolute calibration of the FC. A well defined current from a precise current generator was fed into the circuit of the FC and the data acquisition.

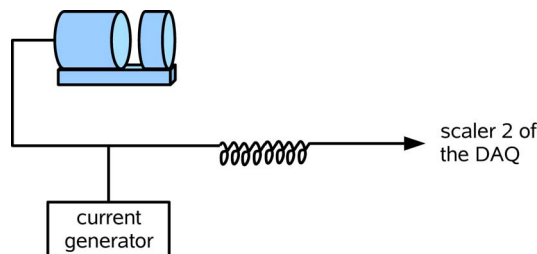


Figure 3.1: Shortly after the exit of the cable from the beam line, the current generator is connected over a T-BNC directly onto the wire, which goes into the electronics and finally into a scaler of the DAQ.

current [ $\mu\text{A}$ ]	Acq. time [t]	scaler content [counts]
1.01	906.04	2.8823E+06
1.16	899.84	3.3282E+06
1.31	899.87	3.7808E+06
1.51	899.84	4.3713E+06
1.81	899.92	5.2699E+06

Table 3.1: *The set current for the calibration measurement and the acquisition time.*

In table 3.1 the different settings of the current generator are listed together with the acquisition time. The chosen range of the current settings reflects the spread of beam currents delivered by the accelerator during the experiment.

The charge in micro Coulomb is given over the multiplication of the acquisition time in seconds with the set current in micro Amperes. The estimated error of the time measurement is less than 0.01 s and the one of the current generator is 0.002  $\mu\text{A}$  at 1  $\mu\text{A}$ . The overall estimated statistical error of the charge is therefore negligible. The recorded scaler counts together with the projected charge were then used to derive a function, which allows to convert the scaler counts of the FC into a charge. The plot of this calibration measurement is shown in figure 3.2.

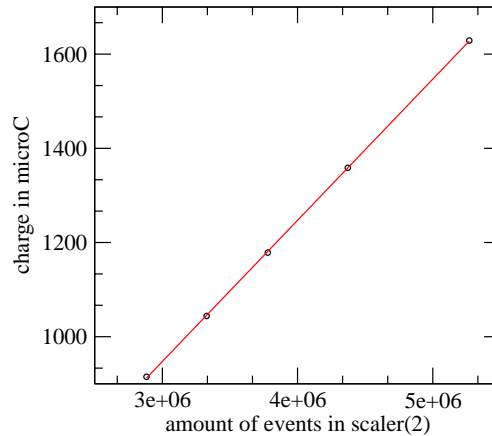


Figure 3.2: *The scaler events of the DAQ are calibrated over a precise accumulated charge. The error bars of the data are negligible small.*

The result of the fit function

$$f(x) = ax + b, \quad (3.1)$$

where  $a$  is the slope and  $b$  is the y-intercept of the curve, is

$$a = 0.000299751 \text{ and } b = 48.101. \quad (3.2)$$

The error matrix is

$$\epsilon = \begin{pmatrix} 2.855E-13 & -1.121E-6 \\ -1.121E-6 & 4.599 \end{pmatrix} = \begin{pmatrix} \sigma_{11}^2 & \sigma_{12}^2 \\ \sigma_{21}^2 & \sigma_{22}^2 \end{pmatrix}, \quad (3.3)$$

where  $\sigma_{11}$  is the variance of the slope  $a$  and  $\sigma_{22}$  the variance of the y-axis intercept. The error matrix 3.3 is then used to calculate the statistical error  $\delta q$  of the charge of the Faraday cup measurement during the experiment over the relation

$$\delta q = \left( \left( \frac{\delta f}{\delta a} \right)^2 \sigma_{11}^2 + \left( \frac{\delta f}{\delta b} \right)^2 \sigma_{22}^2 + 2 \left( \frac{\delta f}{\delta a} \frac{\delta f}{\delta b} \right)^2 \sigma_{12}^2 \right)^{\frac{1}{2}}, \quad (3.4)$$

where the function  $f$  is defined in 3.1. Be  $x$  the recorded scaler counts during a measurement of the beam current via the FC, then from 3.4 follows

$$\delta q = (x^2 \sigma_{11}^2 + \sigma_{22}^2 + 2x \sigma_{12}^2)^{\frac{1}{2}}. \quad (3.5)$$

### Calibration of the iris-setup after the beam chopper

Usually once or twice per day the beam current was measured by inserting the FC into the beam line in front of the target. The recorded counts of scaler(2) of the DAQ allows to calculate the collected charge for the specific run according to equation 3.1 with the fit parameters of 3.2. The collected charge of the FC is plotted then against the scaler counts of the beam iris-setup as shown in figure 3.3 for the data at 1000, 1500 1900 and 2300 keV. The result of the fitted linear curve is superimposed on the represented data.

Beam energy [keV]	Total charge [C]	Stat. error [C]
1000	2.484	0.007
1500	2.259	0.002
1900	0.450	0.005
2300	0.213	0.008

Table 3.2: *Total collected charge*

From the derived parameters of the linear fits and the corresponding elements of the error matrix, the scaler events of the iris-setup can be converted into a total charge in  $\mu\text{C}$ . This has been done for the cumulated scaler counts of the runs of the  ${}^2\text{H}(\alpha,\gamma){}^6\text{Li}$  reaction. The results of the total charge and its statistical error are summarized in table 3.2.



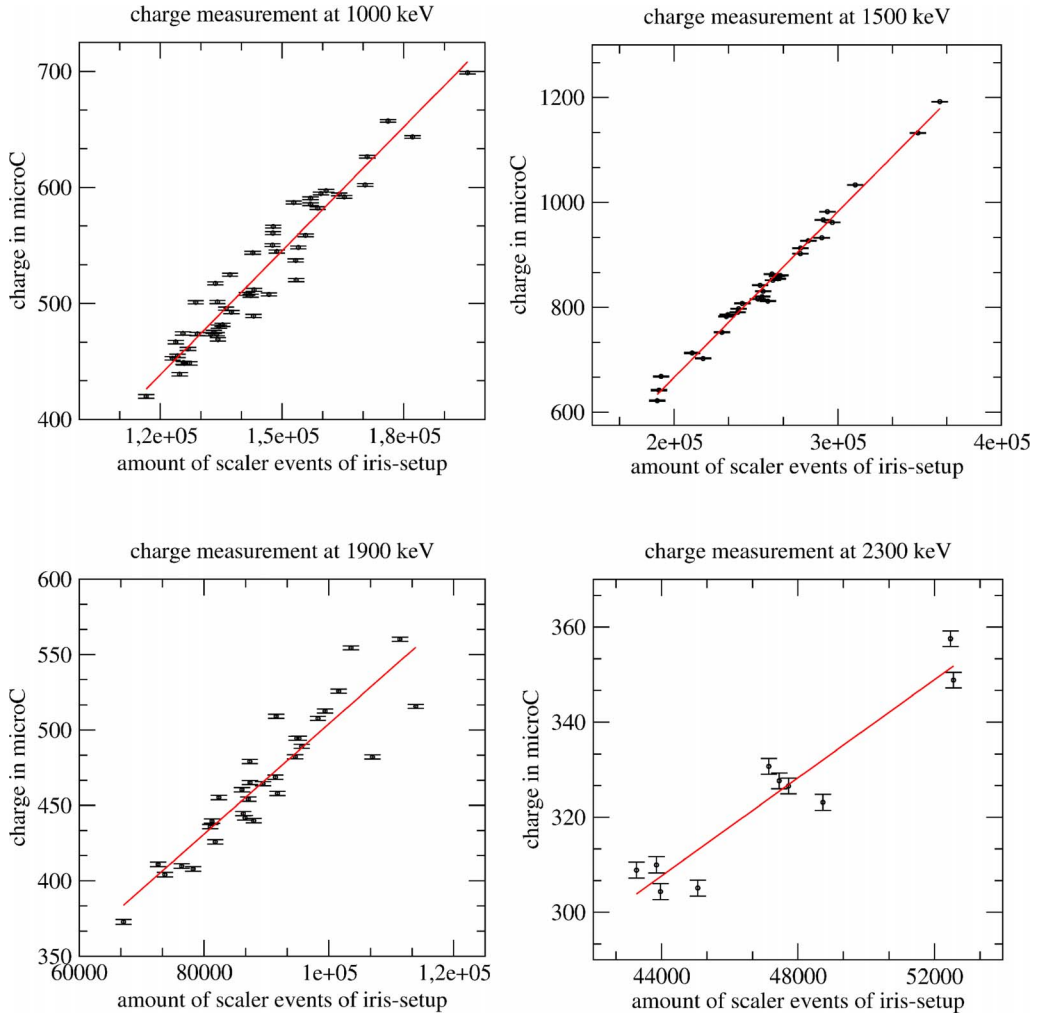


Figure 3.3: The *iris-setup* feeds two scalers of the DAQ. Here the average of the counts of the scalers is plotted on the  $x$ -axis. The  $y$ -axis corresponds to the charge measured by the FC. The statistical error of the data points has been derived by equation 3.5.

## 3.2 Background reactions

Besides the photons of naturally occurring radioactive decays, muons or muon induced particles from cosmic rays are interacting with the detector and generate events, which are not related to the investigated reaction.

Events from cosmic rays can be efficiently suppressed by the cosmic veto (scintillation paddles) and the threshold at the discriminators in the electronics of the data processing. The gammas of the naturally occurring radioactive elements are passively reduced by the lead-copper shielding and the use of low-background materials. In addition the natural background is not time-correlated and can be subtracted from the beam-bunch correlated data of the capture reaction in the offline analysis.

The main background reactions induced by the beam on the target are the

following:

- Photons from the  $^{16}\text{O}(\alpha,\gamma)^{20}\text{Ne}$  capture, where the oxygen is provided by the deuterated water of the target
- $(n,\gamma)$  reactions due to neutrons produced in the target
- Gamma rays from the radioactive decay of activated components of the experimental setup

### 3.2.1 $^{16}\text{O}(\alpha,\gamma)^{20}\text{Ne}$ radiative capture

The Q-value of the  $^2\text{H}(\alpha,\gamma)^6\text{Li}$  is about 1474 keV. This value defines the lower limit of the region of interest in a measured gamma spectrum. However, the energy of the expected gammas of the d- $\alpha$  capture is enhanced by the kinetic contribution of the reaction.

Preliminary studies for the present experiment have shown that the use of deuterated water sets a lower limit to the center of mass energy of the d- $\alpha$  capture. The radiative alpha capture on the oxygen produces photons of 1634 keV, which corresponds to the energy of the photons of the d- $\alpha$  capture at a c.m. energy of 483 keV. Hence, in order to be able to observe the reaction, one has to operate an oxygen-free deuterium target or restrict oneself to a c.m. energy higher than this limit.

Figure 3.4 shows the spectrum of a preliminary measurement with a high purity germanium (HpGe) detector and a frozen normal water target. The  $\text{H}_2\text{O}$

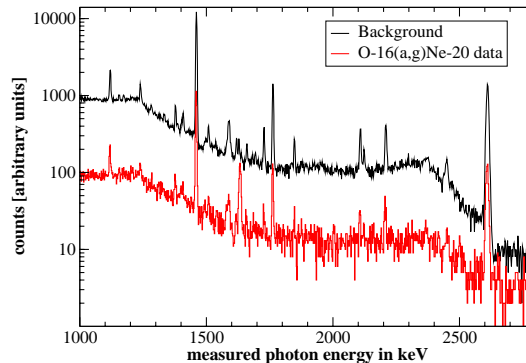


Figure 3.4: *Gamma spectrum measured using a high purity germanium detector. A frozen normal water target was bombarded with 1.5 MeV alphas and the gamma ray line at 1634 keV was measured. The environmental background spectrum, which here has not been scaled down in relation to the acquisition time of the measurement, does only differ by the beam induced gamma ray peak.*

target was bombarded with an alpha beam of 1.5 MeV. The spectrum does not differ from the spectrum of a background measurement of the naturally occurring gammas of the environment except for a gamma line at 1634 keV. According to [29] and [30] the final states of the  $^{20}\text{Ne}$  of the  $^{16}\text{O}(\alpha,\gamma)^{20}\text{Ne}$

capture are all going as the last transition to the ground state through the  $2^+$  transition of 1634 keV.

In contrast to the measurement with the HpGe detector, the measurement of the same reaction with the DaLi setup has by far a higher detection efficiency, due to the larger solid angle. But the energy resolution is worse compared to the germanium crystal. Figure 3.5 shows in comparison to the gamma spectrum of 3.4, the resulting spectrum of the  $\alpha$  bombardment of the  $\text{H}_2\text{O}$  ice target. The spectrum combines the measured events of the crystals 1, 2, 3, 4, 5 and 8. The crystals 6 and 7 have been omitted due to a malfunction of the related TDC channels.

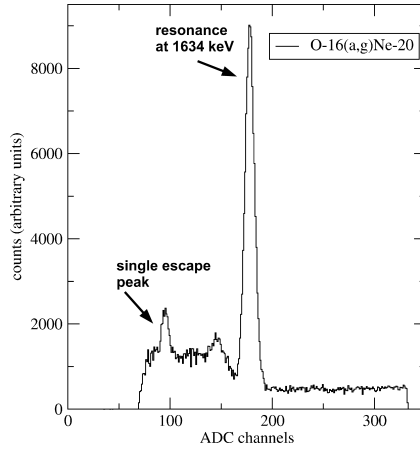
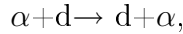


Figure 3.5: *Gamma spectrum of the DaLi detector. A frozen normal water target was bombarded with 1.5 MeV alphas and the gamma ray line at 1634 keV was measured. The contribution of the uncorrelated environmental background has been subtracted from the data. The flat background above the 1634 keV peak originates from gammas of the higher energy levels of the  $^{20}\text{Ne}$ .*

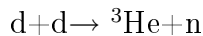
### 3.2.2 Neutron induced background

The most likely reaction between the incident alpha particles of the beam and the particles in the target is the elastic scattering process,



which has no direct effect on the photon detection. However, the elastically scattered deuteron is the source of background.

These deuterons are likely to scatter from other deuterons of the target. This may then cause the reaction



producing 3 to 4 MeV neutrons. Those neutrons can initiate  $(n, \gamma)$  reactions with the materials of the experimental setup. While the gammas from interaction of the neutrons with the material of the detector or the lead-copper

shielding can be discriminated by a time-of-flight discrimination, these gammas produced on the target and target backing can not be distinguished from gammas of the d- $\alpha$  capture.

### $^{16}\text{O}(\text{n},\gamma)^{17}\text{O}$ reaction

According to [39] the photon spectrum of the  $^{16}\text{O}(\text{n},\gamma)^{17}\text{O}$  capture reaction shows lines at 871 and 2184 keV. While the line at 871 keV is below the region of interest and also below the threshold of the discriminator of the DAQ is the line at 2184 keV sitting right in our region of interest. The discussion of the analysis will emphasize this serious issue.

### Neutron activation of the experimental setup

The fast neutrons produced via the deuteron-deuteron reaction have the capability to activate the materials of the experimental setup. The dominant elements of the setup are copper and lead. The crystals of the detector consist of sodium and iodine.

The neutron activation of lead is only possible for the isotope  $^{208}\text{Pb}$  and the lead isotope  $^{209}\text{Pb}$  emits no gammas via its  $\beta$ -decay.

The most energetic gamma line of the radioactive decay of activated copper, either  $^{64}\text{Cu}$  or  $^{66}\text{Cu}$ , is 1346 keV from the decay of  $^{64}\text{Cu}$ , which is indeed below our region of interest.

As for the case of copper, the activated iodine  $^{128}\text{I}$  emits its most energetic gamma of 969 keV below the Q-value of the d- $\alpha$  capture. Activated sodium of the detector crystal can be either  $^{24}\text{Na}$  or its isomer  $^{24m}\text{Na}$ . But only the strong gamma line at 2754 keV of  $^{24}\text{Na}$  may bother the experiment. Although 2754 keV are above the limits of the region of interest and therefore a photopeak is not seen in the gamma spectrum d- $\alpha$  capture, the compton scattered gammas appear in the spectrum, rather as a flat contribution.

Since the half life of  $^{24}\text{Na}$  is 14.96 hours, the radioactive decay is not correlated to the time of the beam bunches. This allows to subtract this background contribution in the offline analysis.

## 3.3 Filtering the data

As already stated the major difficulty of the present experiment is the noise caused by neutron reactions. As shown in figure 3.6 the ADC spectrum of the collected events of the  $^2\text{H}(\alpha,\gamma)^6\text{Li}$  reaction is dominated by background events, hardly any structure can be identified above 1700 keV at the region of interest. The peak at channel 1634 keV derives from the  $\alpha$ -O capture. The narrow peak at 3380 keV is due to the pulser, which is has been fed into the electronics. The edge at 1300 keV derives from the threshold of the discriminator low and the edge at 3400 keV is the limitation set by the discriminator of higher energy events.

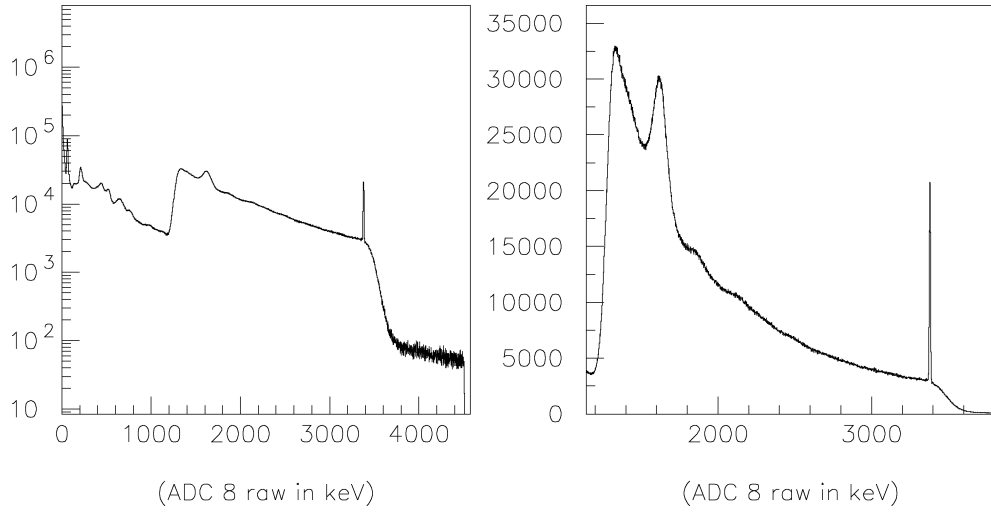


Figure 3.6: *The raw ADC spectrum of channel 8 of the data set at 2.3 MeV. On the left plot the spectrum is shown on a logarithmic scale in counts per keV. On the right plot a part of the plot on the left is displayed on a linear scale.*

Since the beam is bunched a time correlation of the events with the RF of the beam chopper exist. Figure 3.7 shows the TDC spectrum of the recorded events.

The extension of the TDC spectrum is determined by the gate of the

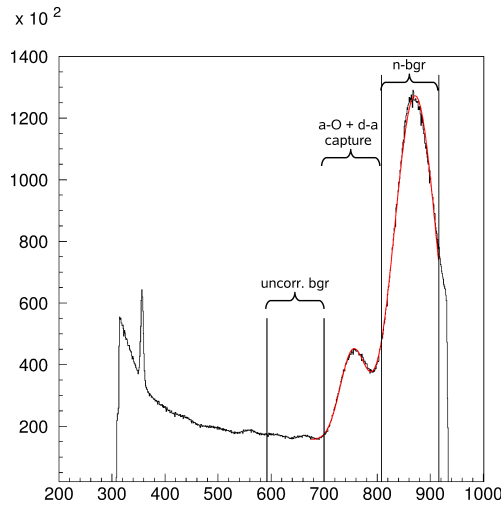


Figure 3.7: *Raw TDC spectrum of channel 8 of the data set at 2.3 MeV. The red curve is a fit of the data assuming for the peaks a Gaussian distribution and for the background a shallow exponential function. The vertical lines represent different regions of interest. The width of the capture time cut is  $\pm 2\sigma$  around the maximum of the derived Gaussian of the small peak in the TDC spectrum. However, in order to increase the signal-to-noise ratio for the final analysis (see section 3.5) a time cut of  $[-2\sigma, +1.5\sigma]$  around the maximum has been chosen. The aspect of the energy dependence of the TDC spectrum is discussed in appendix E.*

coincidence unit of the events and the RF (see screenshot 26 in appendix A).

The time of flight of the gammas to the detector depends on the position of interaction within the crystal of the detector. Since the minimum distance from the target center to the detector is 7.6 cm and the minimum effective radial thickness of the hollow crystal is 8.15 cm, the time of flight of the gammas from the target ranges from 0.25 to 0.53 ns. For neutrons of around 3 MeV kinetic energy it ranges from 3 to 6.5 ns. However, the discrimination via time-of-flight has to take into account the overall time resolution of the experimental setup. As a consequence the events caused by neutron reactions can not fully be discriminated by applying a time cut. Figure 3.7 shows the applied time cut for gammas from the target.

Figure 3.8 shows the result of the ADC spectrum after applying a time cut to select the gammas. The preceding time interval is supposed to render uncorrelated background events.

In addition the data analysis requires that for an event, in order to be

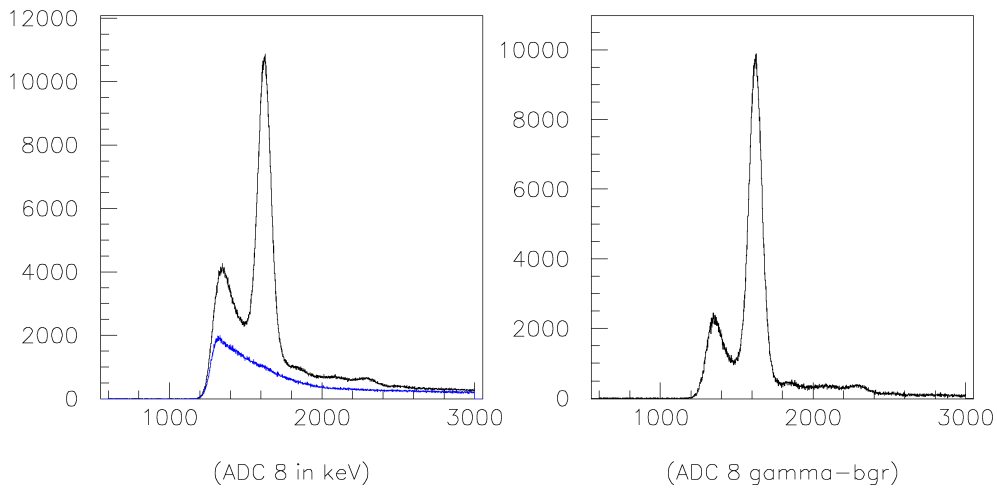


Figure 3.8: *The left picture shows as a black curve the energy spectrum of channel 8 of the events within the time cut for gammas ('gamma-plot'). The ordinate is in counts per keV. The blue curve represents the events of the time cut of the uncorrelated events. The right plot reproduces then the 'gamma-plot' after the subtraction of the uncorrelated background contribution.*

counted as photopeak event, is not allowed to have any other event in another crystal. By this restriction Compton scattered events from one crystal into another one, are discriminated.

The energy spectrum of channel 8 with the time cut, within the range of time of flight of the neutrons, is shown in figure 3.9. In the region of interest between 1600 and 2300 keV, where the events of the d- $\alpha$  capture are expected, the spectrum shows structures, which are due mainly to (n, $\gamma$ )-reaction with the materials of the detector. Since the separation of background events from gamma events of the target is not fully possible, these structures also appear in the 'gamma-plot' as background.

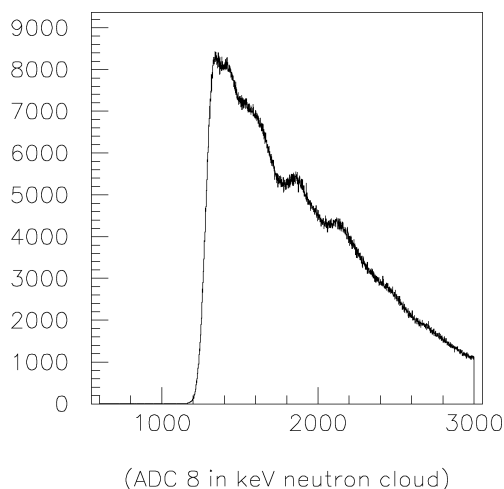


Figure 3.9: *Energy spectrum of the neutron background events.*

### Time dependency of the neutron background

The neutron background represented in figure 3.9 shows in a detailed analysis a time dependency. For this analysis the cut of the neutron background displayed in figure 3.7 has been divided into seven cuts of 0.24 ns each. The ADC spectra corresponding to these cuts are shown in figure 3.10. In order to increase statistics the sum of six crystals of the measurement at 2.3 MeV were used in this background investigation.

Due to the modest time resolution the spectra 6 and 7 in figure 3.10 still

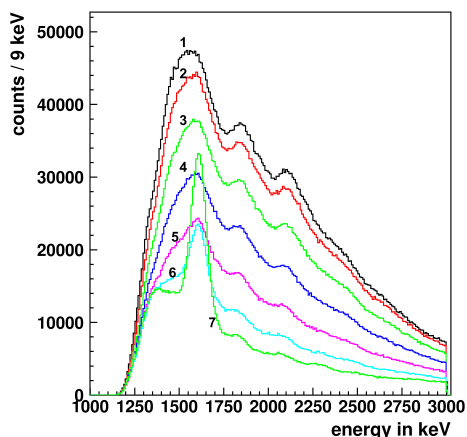


Figure 3.10: *Time dependency of the energy spectrum of the neutron background. The spectra are labeled with numbers from 1 to 7. Spectrum number 7 corresponds to the TDC cut, which is closest to the cut of gammas from the  $\alpha$ -O and d- $\alpha$  capture events.*

contain some events from  $\alpha$ -O and d- $\alpha$  capture reactions, which is emphasized by the peak at 1634 keV from the  $\alpha$ -O capture. Furthermore the spectra show

a rise in slope the further away the TDC cut has been set compared to the TDC position of the time-of-flight of gammas from capture events in the target.

### 3.4 Simulation of the response of the DALI-detector to gamma rays

The interaction between the photons of the d- $\alpha$  capture and the sodium iodine detector is described by two processes:

- compton scattering and
- photo-electric effect.

The simulation of these processes for photons for a wide spectrum of energies has been extensively studied over the last 30 years. Especially the simulation of interactions in the most common used detector crystal, sodium iodide, is the subject of these studies [31] [32]. Monte Carlo simulation codes like GEANT from CERN or EGS4 from SLAC are standard tools in nuclear and particle physics.

For the present experiment the electromagnetic interaction of the photons with the sodium iodide detector has been simulated with the EGS4 code. The simulation includes the geometrical shape of the detector and its copper housing and the tube of the beam line.

#### Photo-peak efficiency

The intrinsic absolute photo-peak efficiency has been calculated using the EGS4 code for two energies corresponding to the gamma rays of the decay of  $^{88}\text{Y}$  at 898 and 1834 keV. The photon source has been modeled assuming isotropic emission as is for the case for the yttrium source used for the experimental determination of the efficiency. The result is tabulated in table 3.3.

<b>Photo-peak [keV]</b>	<b>Efficiency MC [%]</b>	<b>Efficiency Exp. [%]</b>	<b>Ratio MC/Exp</b>
898	36.4	30.3	1.20
1834	23.5	19.75	1.19

Table 3.3: *The simulated photo-peak efficiencies (MC) are compared to experimental values (Exp).*



The comparison between the simulation and the experimental values of table 2.2 shows a disagreement up to 20%. The reason of this large discrepancy could not be determined. Systematic errors like misalignment of the source in the detector or a false activity of the calibrated source are not likely to explain this effect. However, since the discrepancy behaves like a proportional enhancement, the intrinsic efficiency of the simulation has been manually adjusted according to the experimental values of table 2.2 in the further analysis.

### Simulated photon spectrum of the d- $\alpha$ capture reaction

The energy of the photons at the center of the detector is of course dependent on the kinetic energy of the incident alpha particle onto the deuterated water target. In addition the energy loss of the alpha particle in the target has to be taken into account for the generation of the photon source of the EGS4 simulation.

This energy loss has been calculated using the stopping power data of helium ions in condensed water of the ASTAR code provided by NIST [33]. The data of ASTAR are derived from fitting-formulas which are based on experimental stopping power data. According to [33] and [36] the uncertainties are estimated to be 2% to 5% at 1000 keV, 5% to 10% at 100 keV, 10% to 15% at 10 keV, and at least 20% to 30% at 1 keV. The large uncertainties at low energies are not worrying, since the contribution of these low-energy alphas to the integrated total cross section of the d- $\alpha$  capture is very low. However, since the cryogenic target consists of D<sub>2</sub>O ice, the stopping power data of H<sub>2</sub>O have been corrected for the isotopic difference as for the density of water ice compared to the liquid phase. The overall conversion factor of the condensed water data of ASTAR to deuterated water ice values is 0.897, which is consistent with available experimental electronic stopping power data of protons in normal [34] and deuterated [35] water ice media.

In order to calculate the luminosity of the incident alpha beam with the target, the kinetic energy of the alpha particle is first divided into discrete quantities  $dE$ . Via the corresponding stopping power a discrete range  $dx$  in the target is determined, which allows then to calculate the luminosity. Hence, the photon energy, which is derived from the kinematics of the  ${}^2\text{H}(\alpha,\gamma){}^6\text{Li}$  reaction, is of discrete energy value too.

The simulation generates via a random seed a distribution of photons, of which the energy is given by the Q-value and the kinematics of the d- $\alpha$  reaction. The code also takes the probability of the radiative capture of the single event into account. This probability, which is implemented into the code, is derived from the theoretical cross section calculation of Nollett shown in figure 1.6.

The experimental angular distribution of the photon from the d- $\alpha$  capture is not isotropic. Hence this effect has to be implemented into the simulation

too. The distribution of the photons is determined by the E2 transition near the resonance, but E1 becomes also important at lower energies. This energy dependence of the angular distribution of the emitted photons has been studied by K. M. Nollett [37] and has been implemented into the simulation. The result of the simulation for one single crystal is represented in figure 3.11. The calculated spectrum has been obtained for three different detector resolutions.

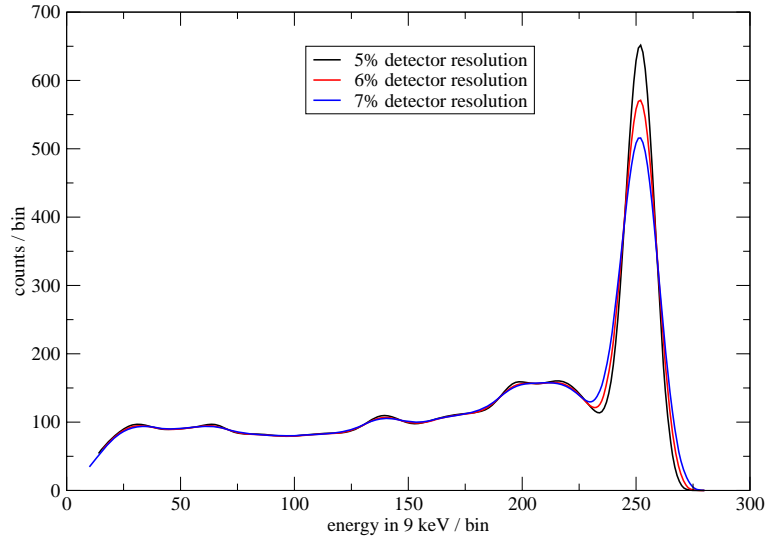


Figure 3.11: *Simulated response of one crystal of the DaLi detector to photons from the  $d$ - $\alpha$  capture. The abscissa shows the photon energy binned in 9 keV and the ordinate the counts per bin. The incident alpha particles have a kinetic energy of 2.3 MeV.*

### 3.5 Comparison of the 2.3 MeV data to simulation

As for the analysis of crystal number 8 in section 3.3 the same filtering procedure is applied to the data of the remaining crystals and the resulting spectra are combined. The subtraction of uncorrelated background as suggested in figure 3.8 has not been performed. This because a careful analysis of the so-called uncorrelated region (see TDC spectrum in figure 3.7) showed nevertheless some little correlation, which was not understood.

Due to technical problems two crystals (No. 6 and 7) have not been included into the final analysis. Number 6 had a bad TDC channel, which impedes a time-of-flight analysis, and number 7 showed very large gain shifts of the photomultiplier, which could not be corrected in the analysis. The experimental result of the cumulated events of 6 crystals is represented in figure 3.12.

The simulated response (5% energy resolution) for six crystals and 0.213 C beam charge is shown as the black hatched curve on the insert plot in figure 3.12. Additionally, the spectrum of the simulation has been adjusted to ac-

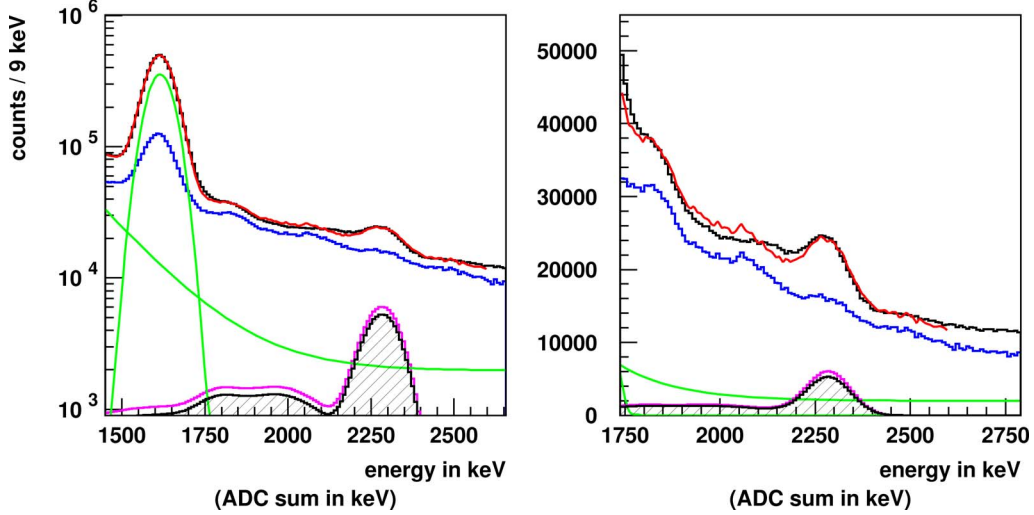


Figure 3.12: *Experimental result of the cumulated events of six crystals (black histogram) compared to the simulation with EGS4 (hatched histogram). The green curves on the plots show the fitted exponential term ( $f = Ae^{-Bx} + c$ ) of a generic background and the  $\alpha$ -O capture peak approximated by a Gaussian. The blue line represents the contribution from  $(n,\gamma)$  reactions and the magenta histogram represents the spectrum of the simulation scaled by the fit.*

count for the experimental photo-peak efficiency of the detector. Therefore the spectrum of the simulation has been scaled by a factor of 0.84 (see section 3.4).

Another correction has been applied because of the loss of statistics due to cuts in the time-of-flight. Instead of a TDC cut as proposed in figure 3.7 of  $\pm 2\sigma$  a cut with a width of  $3.5\sigma$  (from  $-2\sigma$  to  $+1.5\sigma$ ) has been chosen, which corresponds to a correction factor of 0.91. The correction due to the experimental dead time of 17.1% is given by a scaling factor of 0.829. The comparison between the experimental energy spectrum of the analysis and the EGS4 simulation of the response of the detector is performed by a fit, which also accounts for different background contributions.

The prominent peak at 1634 keV is due to the  $^{16}\text{O}(\alpha,\gamma)^{20}\text{Ne}$  capture reaction. Other sources of background derive from the interaction of neutrons with the detector, target and its holder. The contribution of these reactions in the energy spectrum can be approximated by a superposition of a spectrum derived from the analysis of events, which have a larger time-of-flight compared to the one of gammas. In the proposed fit the shape of this spectrum is allowed to scale freely in height.

The derived scaling factor  $\zeta$  for the spectrum of the simulation is

$$\zeta = 1.14 \pm 0.09.$$

The reduced  $\chi^2$  of the fit is 0.46. The given error is mainly due to the uncertainty of the charge measurement.

### Discussion of the fit result

With a value of  $\zeta$  around 1.14 and the corresponding statistical error of  $\pm 0.09$  the present thesis has shown the feasibility of a thick target experiment of the d- $\alpha$  capture reaction. However, the method could not be applied to lower energies because of the presence of oxygen in the target.

Besides of the statistical error the systematic errors need also to be discussed. For the case of the experiment three major sources of systematic errors can be postulated:

- impurity deposition on the cryogenic target and subsequent loss of luminosity
- miss-calibration of the beam charge
- contamination of the  $\gamma$ -spectrum with events from (n, $\gamma$ ) reactions

The issue of the impurity would result into a lower rate of the capture reaction and hence the factor  $\zeta$  of the fit of the experimental spectrum would become smaller than expected. But since the beam was hitting the target without any considerable interruption, the heat load prevented any undesired deposition on the target. In addition the regular refreshing of the target produced every time a new layer of pure deuterated water ice.

An underestimation of the total charge of the beam would result in an enhancement of  $\zeta$ . But considering the careful calibration of the beam charge measurement, a large systematic error is unlikely.

More likely, as the analysis of the neutron background shows, the possibility of an overestimation of the cross section is due to a contribution of events from (n, $\gamma$ ) reactions, which can not be separated from d- $\alpha$  capture events.

According to [39] the photon spectrum of the  $^{16}\text{O}(n,\gamma)^{17}\text{O}$  capture reaction shows lines at 871 and 2184 keV. One can see that the proposed fit in figure 3.12 exactly fails at the photon energy around 2184 keV, which is indicating a possible slight overestimation of the cross section.

## 3.6 Analysis of the data at 1.9, 1.5 and 1.0 MeV

The analysis of the data at the incident  $\alpha$ -energy of 1.9, 1.5 and 1.0 MeV was not successful. Due to the kinematics the photon energy of the d- $\alpha$  capture reaction drops to lower values compared to the resonance photons. As a consequence the photon peak of the d- $\alpha$  capture reaction at lower energies is overlaid with the peak at 2184 keV of the  $^{16}\text{O}(n,\gamma)^{17}\text{O}$  and other structures from (n, $\gamma$ ) reactions, which prevent to derive any useful information regarding the cross section.

# Chapter 4

## Conclusion

Although the understanding of the early universe has been improved by the recent results of the WMAP mission, the measurement of the cross section of the  ${}^2\text{H}(\alpha,\gamma){}^6\text{Li}$  is still of interest to rule out theoretical uncertainties of the results from indirect breakup measurements. Consequently, the theoretical calculation of the cross section can be validated at those energies, where the influence of different nuclear transitions becomes more important.

The DaLi-project is characterized by many technical problems, which were solved starting from scratch. The feasibility of a thick target experiment for this reaction has been demonstrated for the resonance. While the calculation of a final cross section depends on the outcome of a Monte Carlo simulation, this method, thanks to the enhancement of luminosity by the employment of a solid target compared to a gas-jet target, allows to investigate the cross section at low energy. It is worthwhile to mention that the use of a pure deuterium target would increase the luminosity by a factor of three with respect to deuterated water ice. But the refrigeration of deuterium should be realized by a liquid helium flow and not by an expander as used at the beginning of this experiment. The limitation of the cooling power of the expander proved to be a problem. The fact that a liquid helium cooling allows a compact design, as realized for the cryogenic water ice target, makes liquid helium cooling the preferred option.

The analysis shows that the choice of materials of the experimental setup and a good time-of-flight resolution is crucial for the success of the experiment. Future experiments should be aware of this issue and may also benefit from the investigation of the background reactions. Since the time of flight of neutrons depends on their kinetic energy and the distance of the target to the detector, it is suitable to increase this distance for a better noise to background separation.

Moreover the detector type could be chosen considering a better energy resolution. The drawback for most detector materials, with better energy resolution than NaI(Tl) is that the intrinsic time spread of the signal is larger and hence requires a larger distance to the target.

# Appendix A

## Schematic setup of the electronics

The content of appendix A shows first five schematic drawings of the electronics. Then the drawings are followed by the screenshot pictures of the oscilloscope at a given position in the electronics. The screenshot pictures are labeled with a number, which corresponds to the number enclosed in a circle in the drawing of the electronics such as ①, where ‘a’ is an integer number. The tables below summarizes the pictures of the drawings and screenshots.

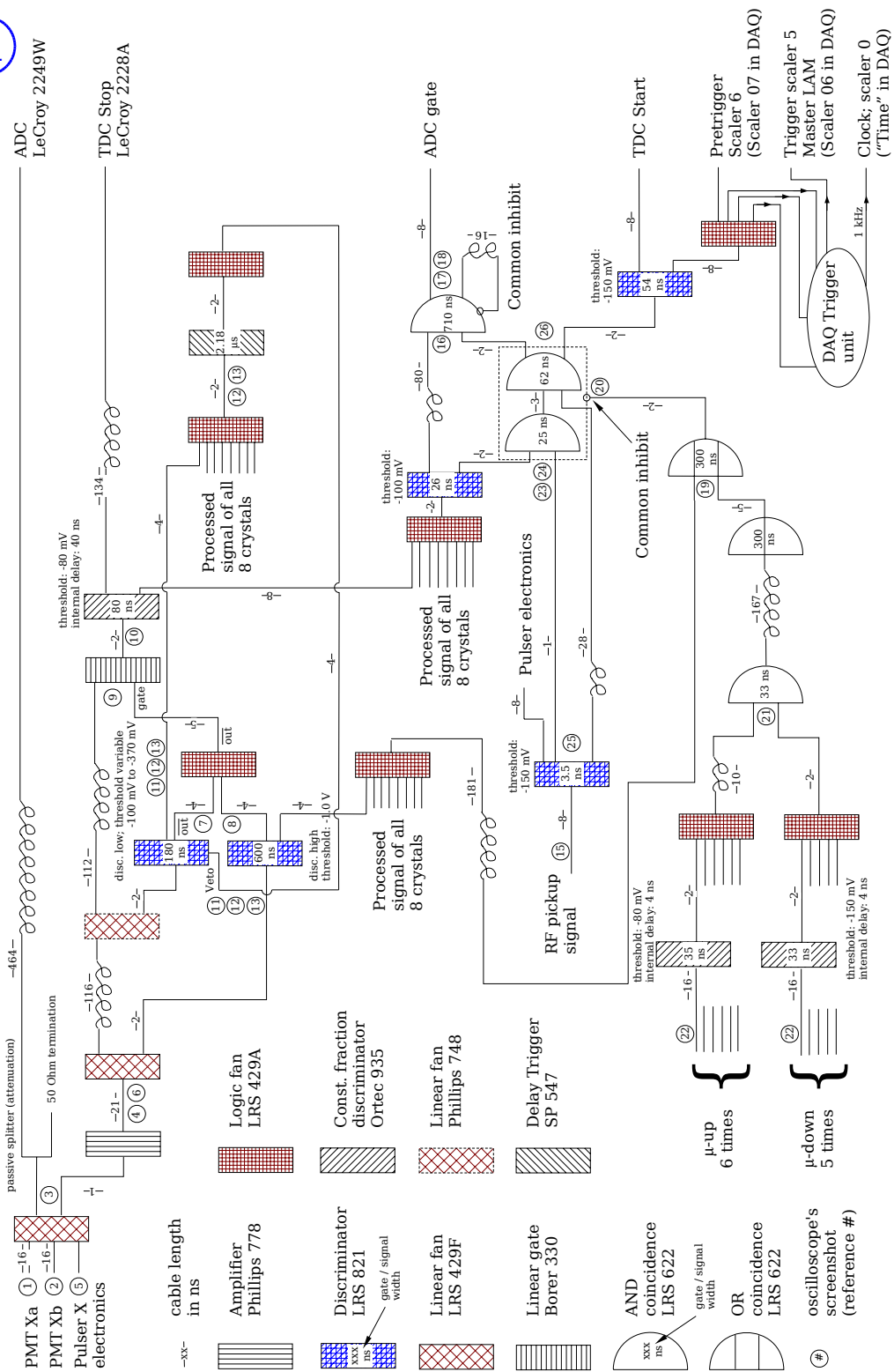
Picture ID	Comments
A	Main logic of the electronics of the experiment
B	Electronic setup for generating pulser signals
C	Electronic setup for picking up the RF signal and setup for the detection of backscattered $\alpha$ -particles
D	Setup of the measurement of the beam current; absolute (Faraday cup) and relative (chopper slit)
E	Electronic setup of the measurement of the time structure

Picture ID	Comments
1	PMT4a (HV -1010 V): Signal height of a Co-60 source
2	PMT4b (HV -1035 V): Signal height of a Co-60 source
3	Combined PMT signals of tube 4 after LRS 429F
4	Combined PMT signals of tube 4 after amplifier Phillips 778
5	Pulser signal for tube 4 before entering the main electronics
6	Pulser signal for tube 4 after amplifier Phillips 778
7	Channel 1: discriminator high (cosmic event!) Channel 2: discriminator low, inverted out
8	Channel 1: no signal Channel 2: with signal; this means event was not a cosmic's
9	Amplified PMT signal that goes into 'borer lin. gate' and the gate which opens the 'borer lin. gate' out channel
10	Signal coming out of the borer lin. gate and going into CFD
11	Tight signal: normal out of discriminator low Broad signal: veto signal that acts on disc. low Veto is generated by a delay trigger. width: 2.18 microsec
12	Channel 1: disc low of tube 5 Channel 2: veto for disc. low Channel 3: Logic Fan out that contains all 8 disc. low signals Channel 3 shows two pulses. The first one is generated by tube 5. The second pulse comes from a tube of the remaining seven ones.
13	Channel 1: disc low of tube 5 Channel 2: veto for disc. low Channel 3: Logic Fan out that contains all 8 disc. low signals Channel 3 shows one pulse. The first one is generated by tube 5. The second pulse comes from a tube of the remaining seven ones.
14	RF signal after the passive splitter
15	RF signal after the frequency doubler
16	Channel 1: The 8 CFDs go into a logic FAN and then the out goes into a discriminator in order to reshape the signal. One out of this discriminator goes into a coincidence with the RF. The second out of this discriminator is on channel 1 of the oscilloscope. Channel 2: The RF performs a double coincidence. The first time the coincidence is with the signal of a CFD. This coincidence signal performs then again a coincidence with the same, but delayed RF signal. The output of this double coincidence is on channel 2 of the oscilloscope.

Picture ID	Comments
17	<p>Channel 1: Signal for ADC gate coming out of the last coincidence unit.</p> <p>Channel 2: Same signal as channel 1 but delayed by 16 ns. This signal goes as common inhibit into its generating coinc. unit.</p>
18	<p>Same constellation as for picture 19, but time scale is smaller. 'zoom' of picture 17</p>
19	<p>Channel 1: Signal coming from the cosmics-electronics</p> <p>Channel 2: Discriminators high goes into a logic Fan. The out of the Fan is channel 2 of the oscilloscope.</p> <p>The two signals (ch1 &amp; ch2) go into an 'OR'-coincidence and the resulting out acts then as common inhibit at the double coincidence unit of the RF. When ever a cosmics strikes, the event is cancelled.</p>
20	<p>Channel 1: Common inhibit signal for the RF-coinc. unit</p> <p>Channel 2: Signal-out of the first coincidence of an event with the RF</p>
21	<p>Channel 1: All six signals of the cosmics-up discriminators go into a logic Fan. The out of the Fan (a little bit delayed) is on channel 1 of the oscilloscope. The delay is needed to perform afterwards a coincidence with the cosmics paddles 'down'.</p> <p>Channel 2: Cosmics-down (signal from logic Fan)</p>
22	<p>Channel 1: Detector 4 of a cosmics-up. PMT signal.</p> <p>Channel 2: Detector 1 of a cosmics-down. PMT signal.</p>
23	<p>Channel 1: Signal of the RF</p> <p>channel 2: Random events from the CF discriminators, which are grouped into a logic Fan.</p>
24	<p>Same condition as in 23, but larger time scale.</p>
25	<p>RF signal before entering the coinc. unit together with an event.</p>
26	<p>Channel 1: Delayed RF signal</p> <p>Channel 2: Signal of the event-RF coincidence before going into the second coincidence with the delayed RF.</p>

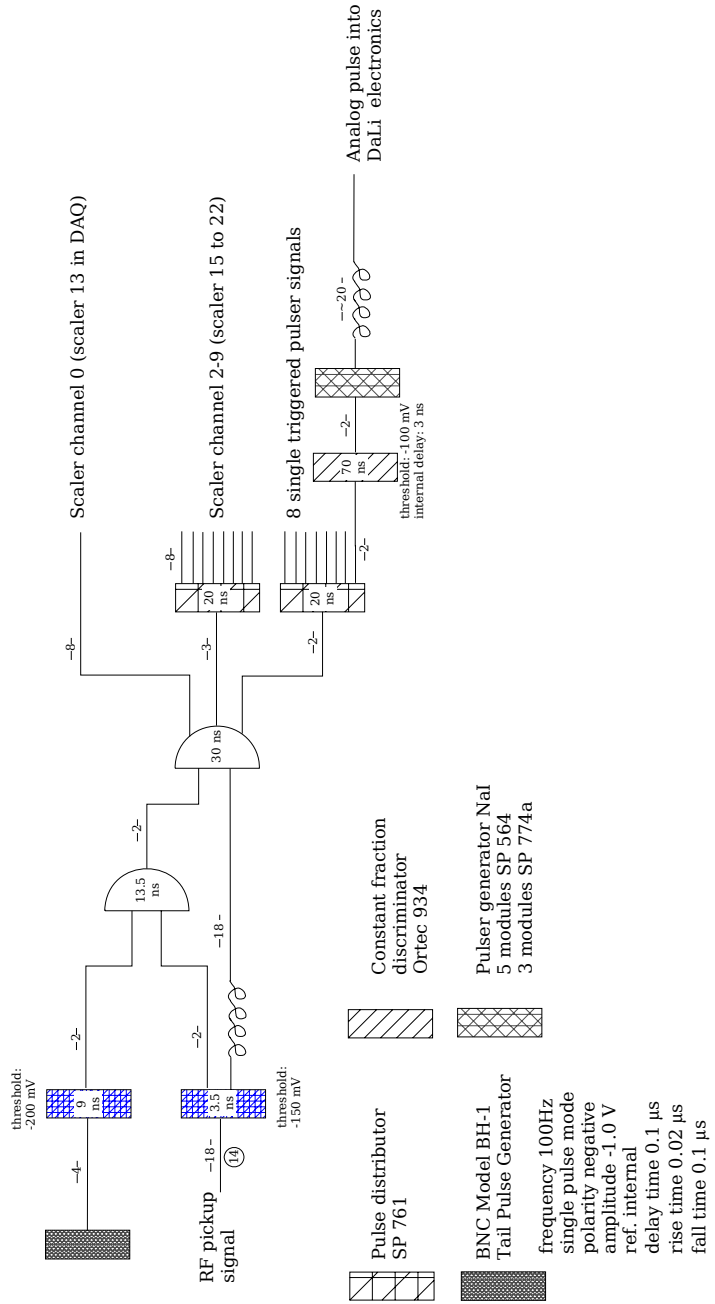


# Electronic setup of the DaLi experiment

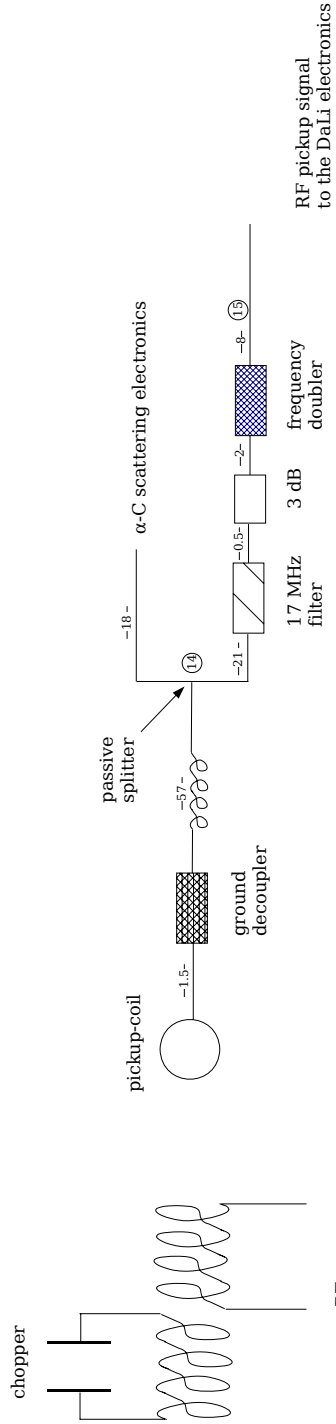


## Electronic setup for generating pulser signals

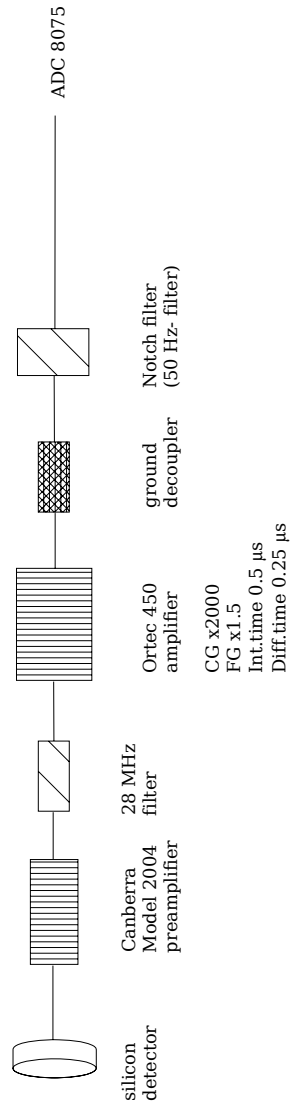
B



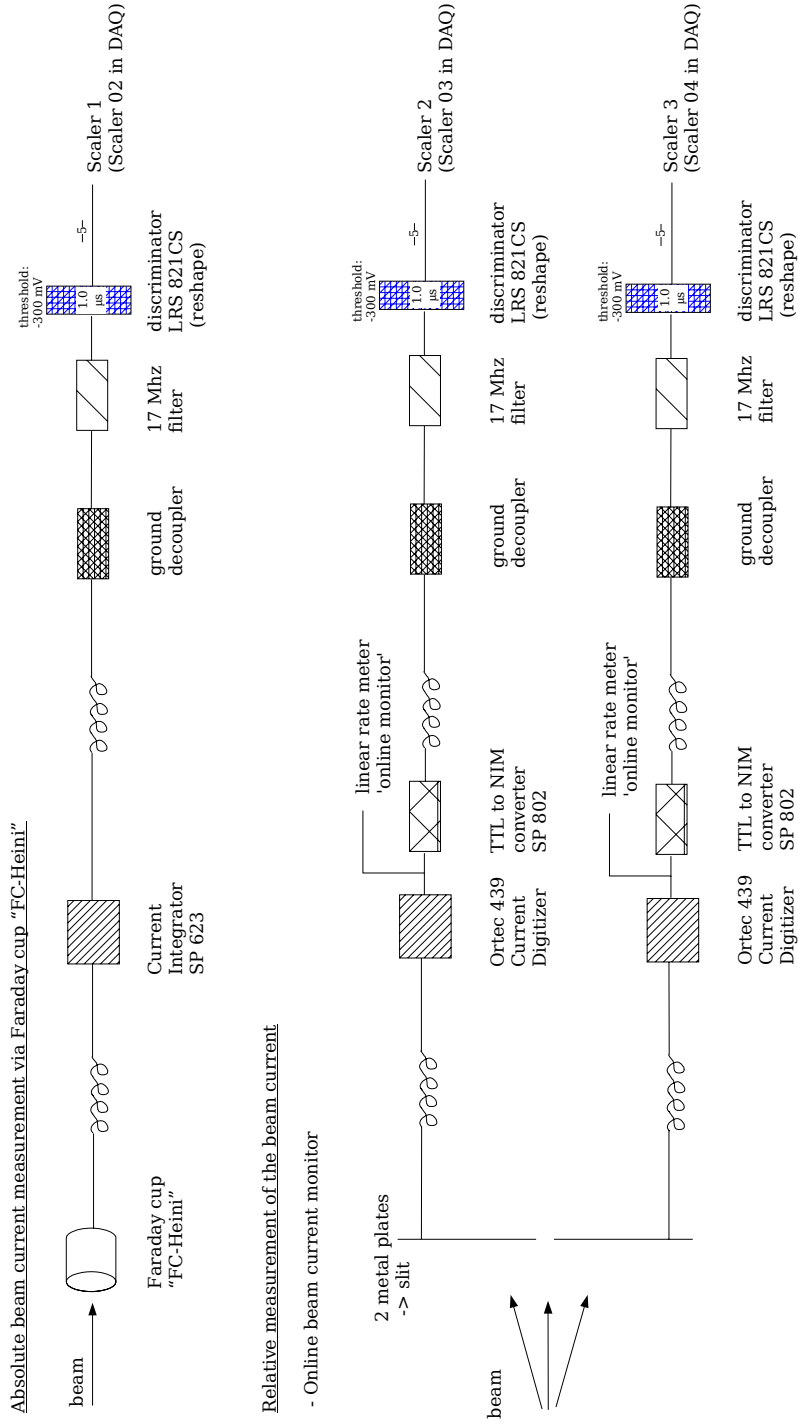
Pickup of the RF-signal of the beam chopper



Setup of the electronics for the back scattered  $\alpha$ -particles

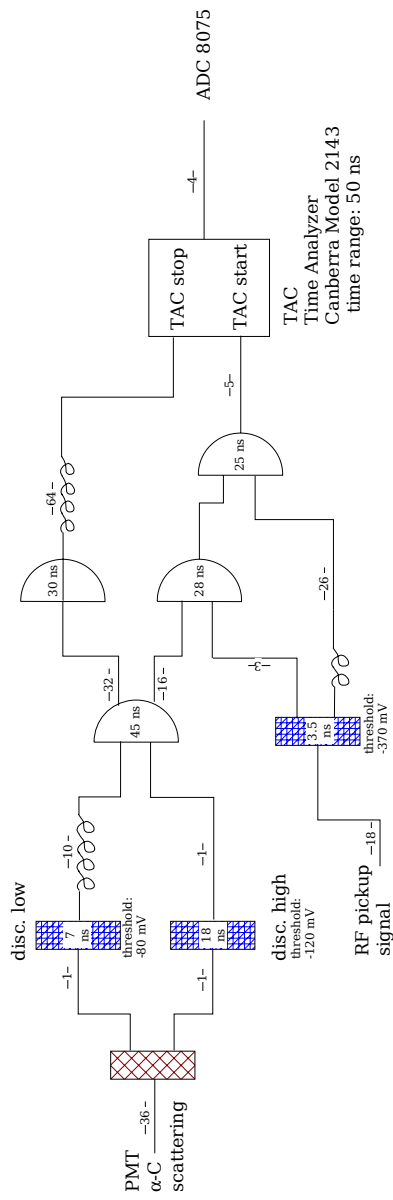


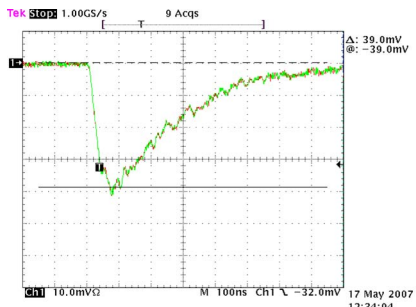
## Electronic setup for measuring and monitoring the beam current



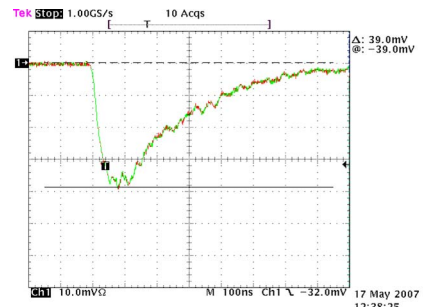
Electronic setup for the detection of  $\alpha$ -C scattering

Measurement of the time structure of the beam

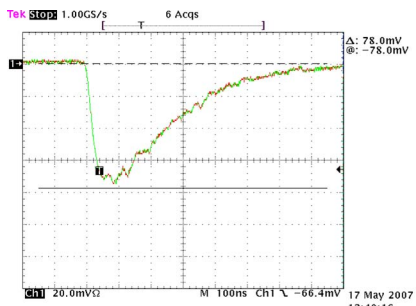




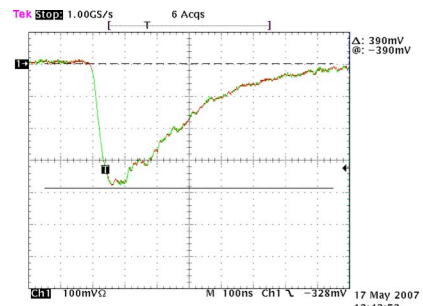
Screen shot number 1



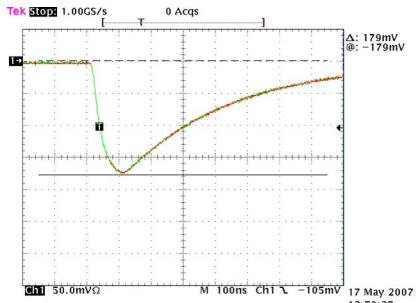
Screen shot number 2



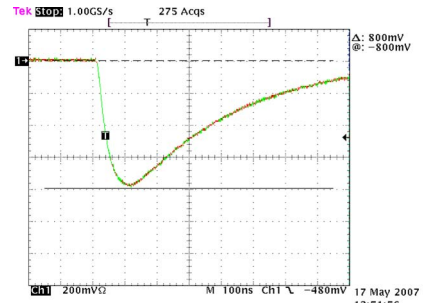
Screenshot number 3



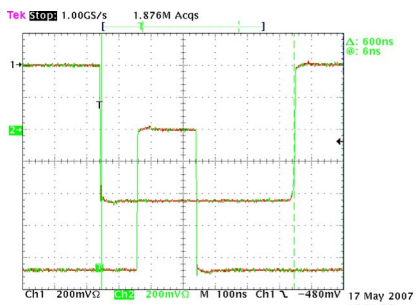
Screenshot number 4



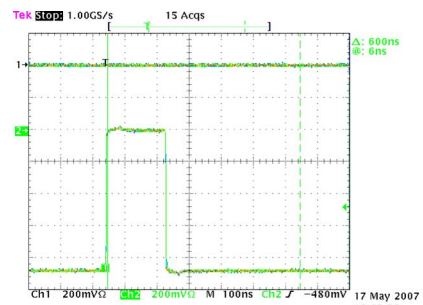
Screenshot number 5



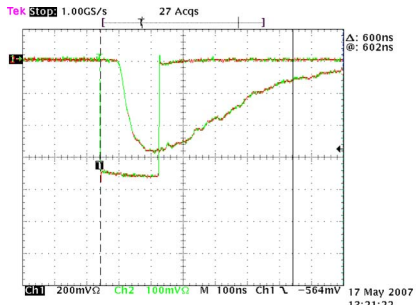
Screenshot number 6



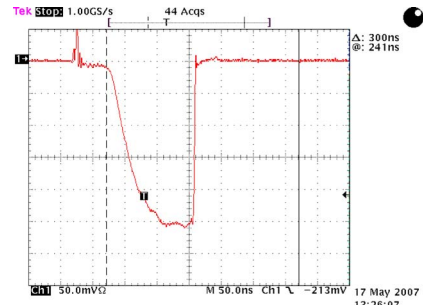
Screenshot number 7



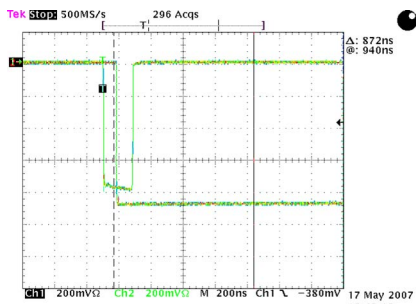
Screenshot number 8



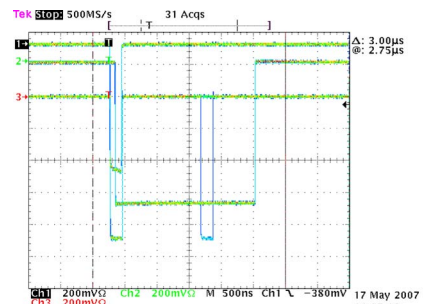
Screenshot number 9



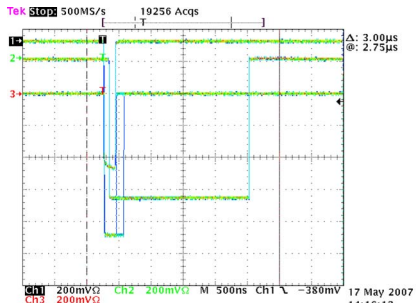
Screenshot number 10



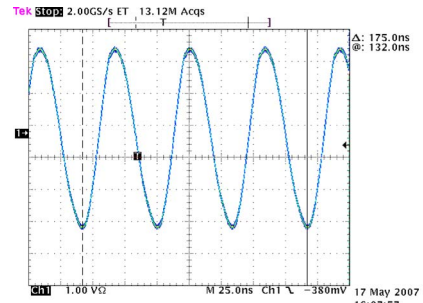
Screenshot number 11



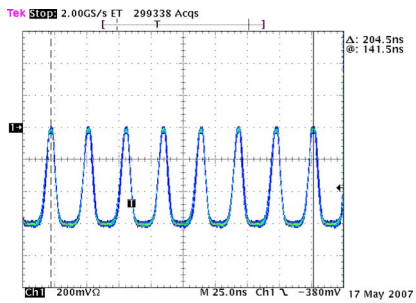
Screenshot number 12



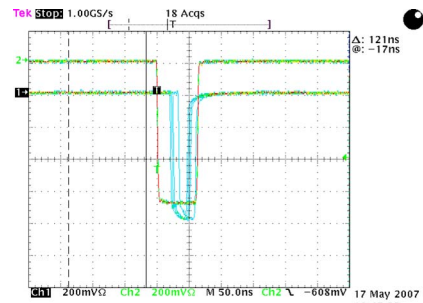
Screenshot number 13



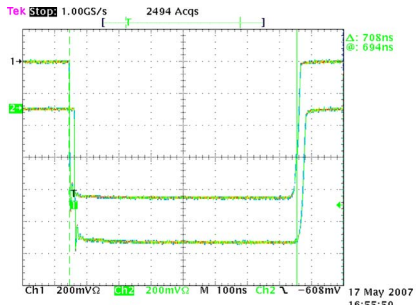
Screenshot number 14



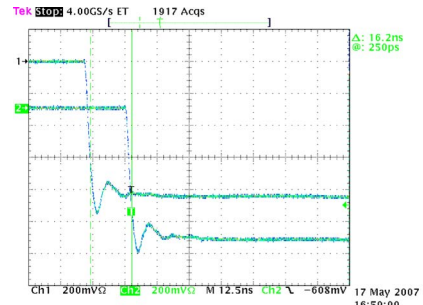
Screenshot number 15



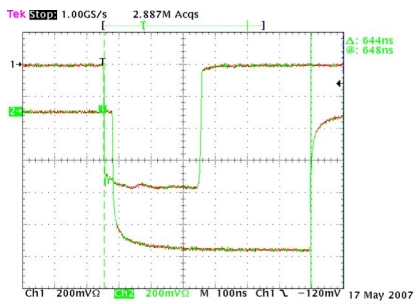
Screenshot number 16



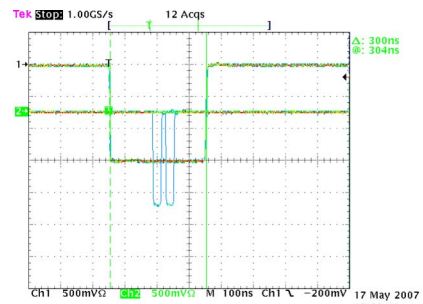
Screenshot number 17



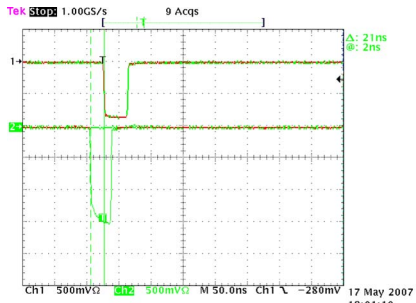
Screenshot number 18



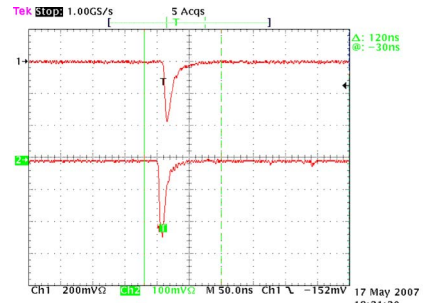
Screenshot number 19



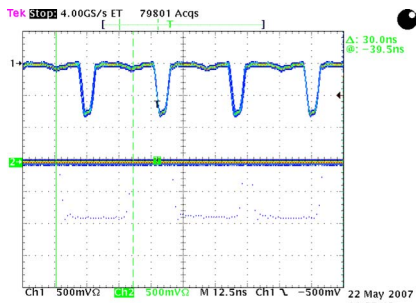
Screenshot number 20



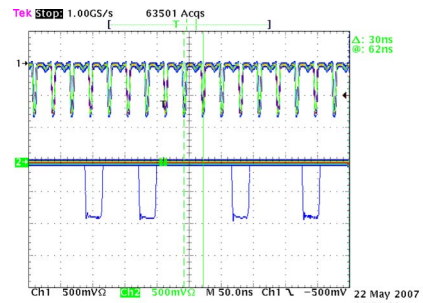
Screenshot number 21



Screenshot number 22

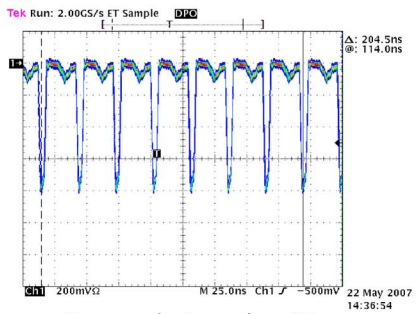


Screenshot number 23

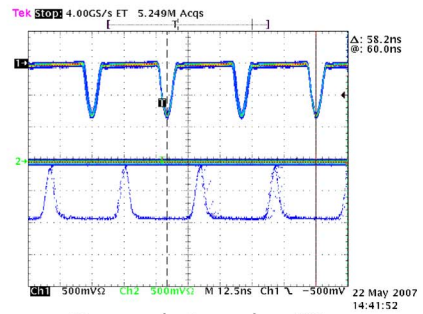


Screenshot number 24





Screenshot number 25

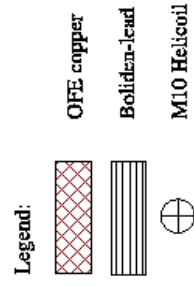
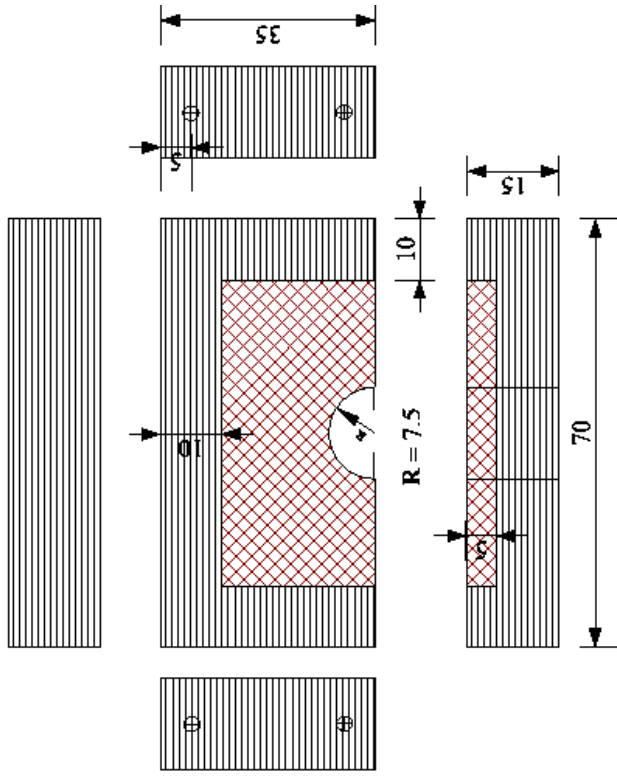


Screenshot number 26

## Appendix B

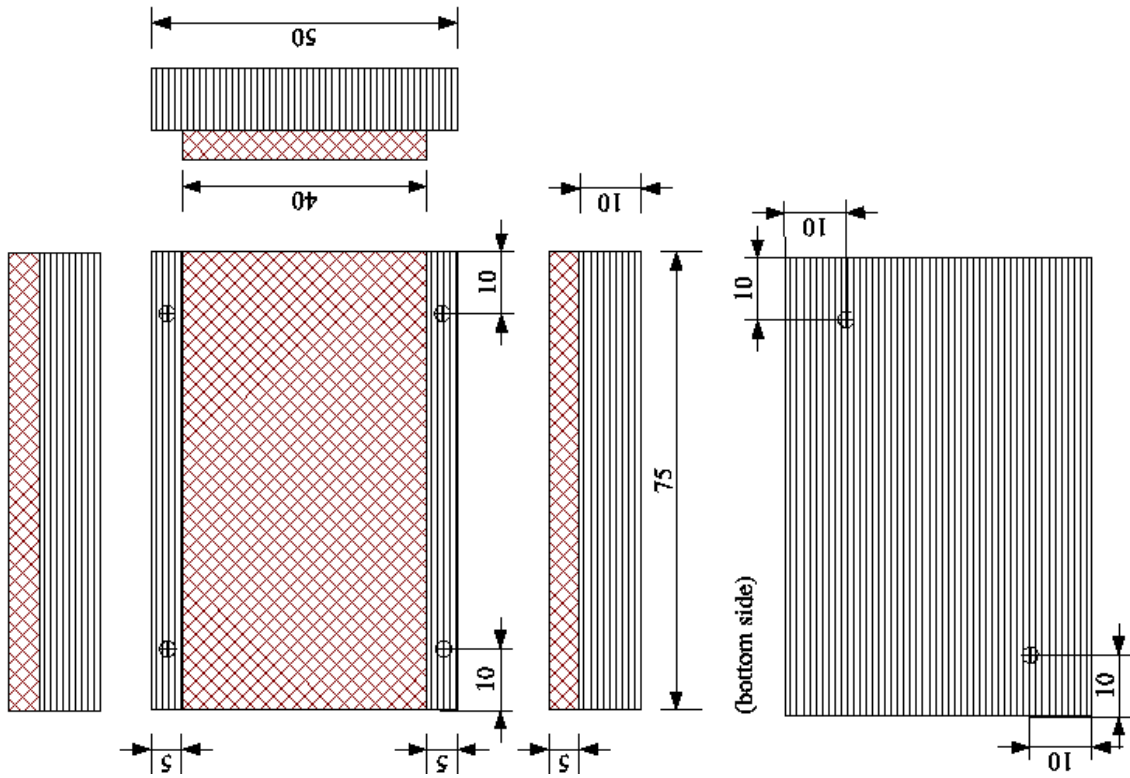
### Technical Drawings of the DaLi shielding

Lead door (4 halves)

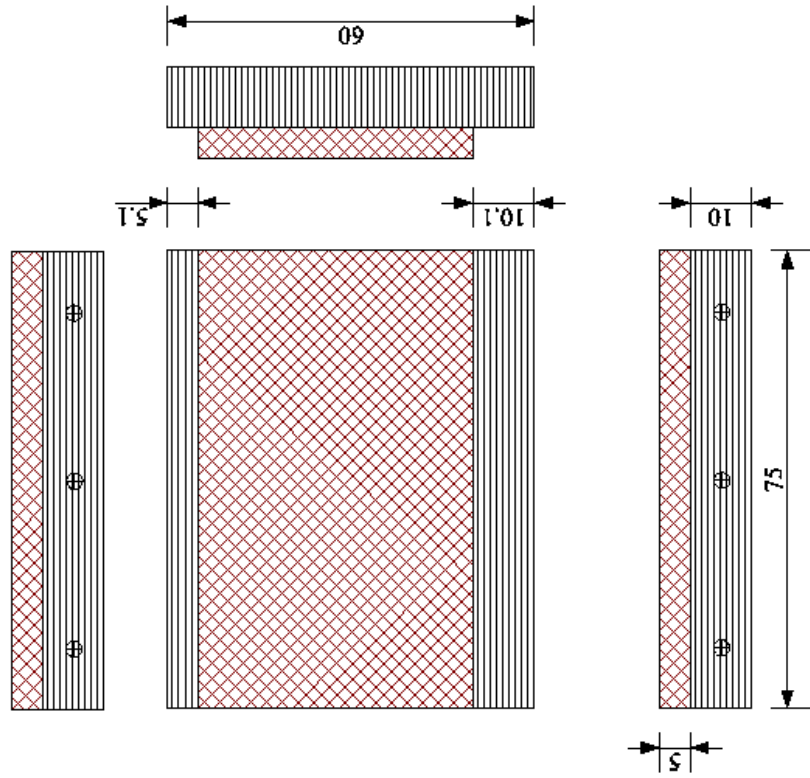


All values in cm.  
 The copper shielding consists of two plates. The plate underneath is 3 cm and the upper one is 2 cm thick.

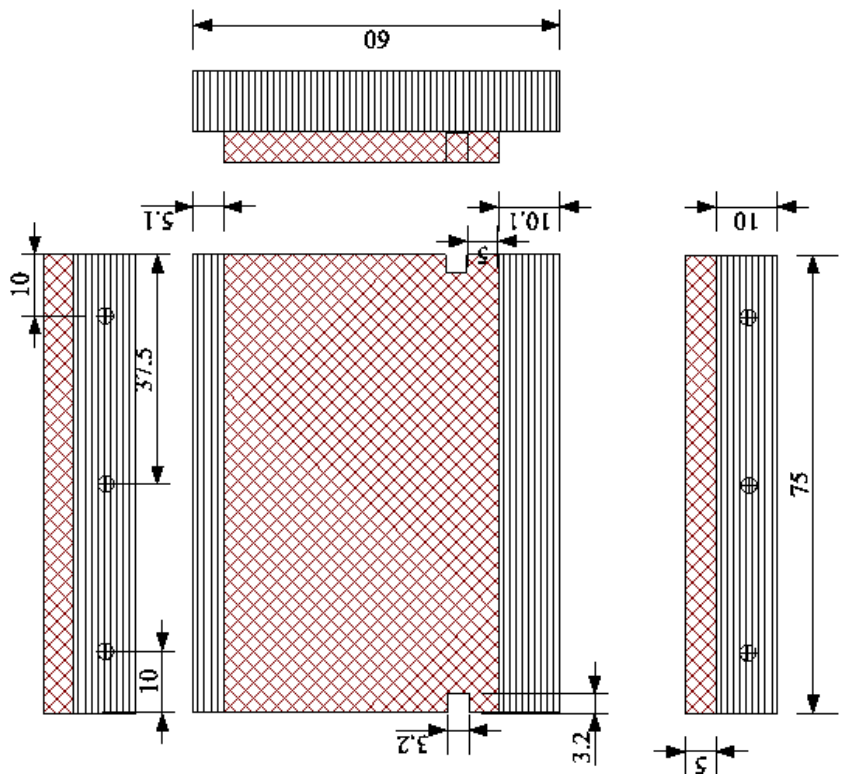
Base plate

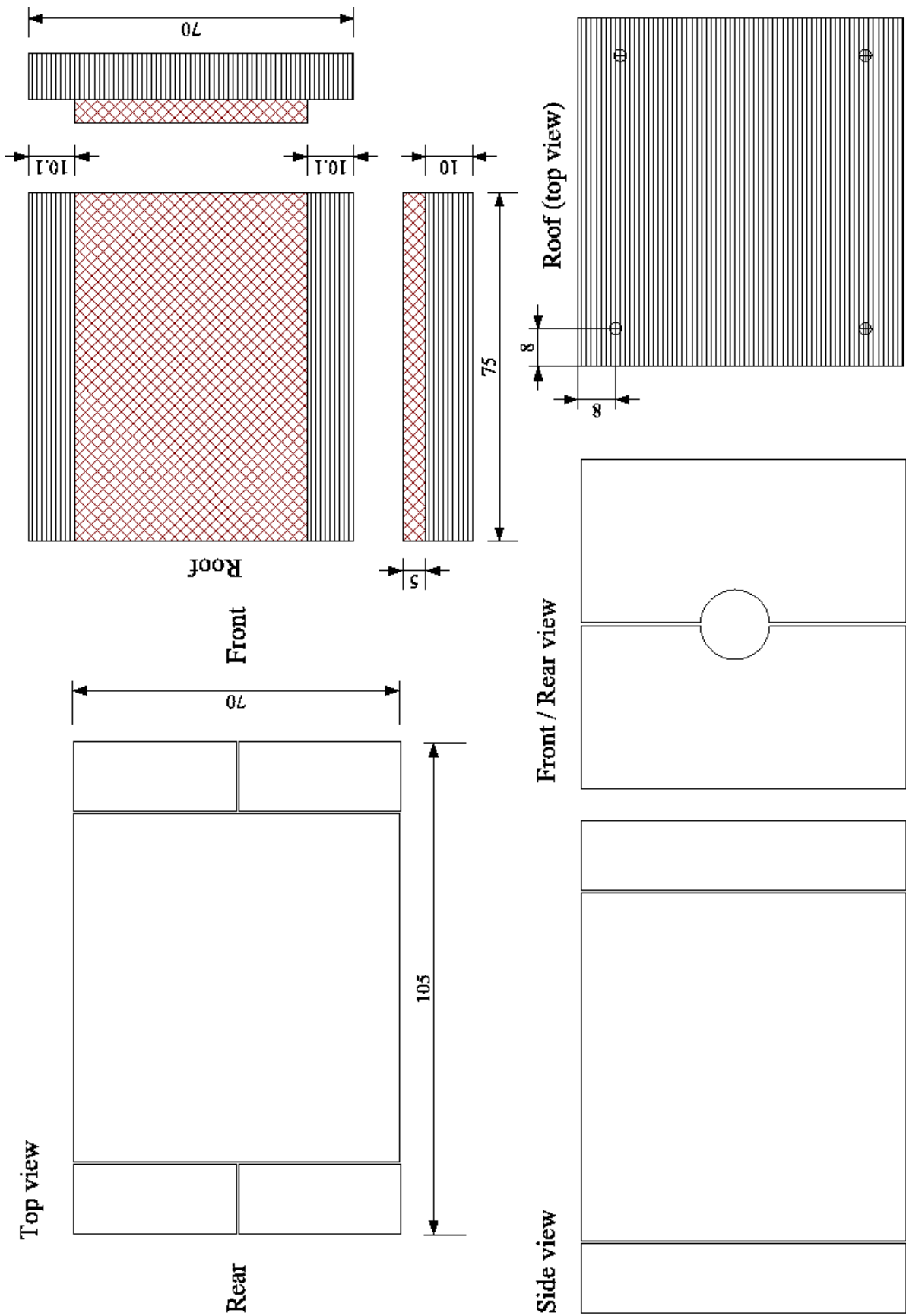


Side wall right



Side wall left





## Appendix C

### Greinacher-style multiplier for the 4 MV accelerator

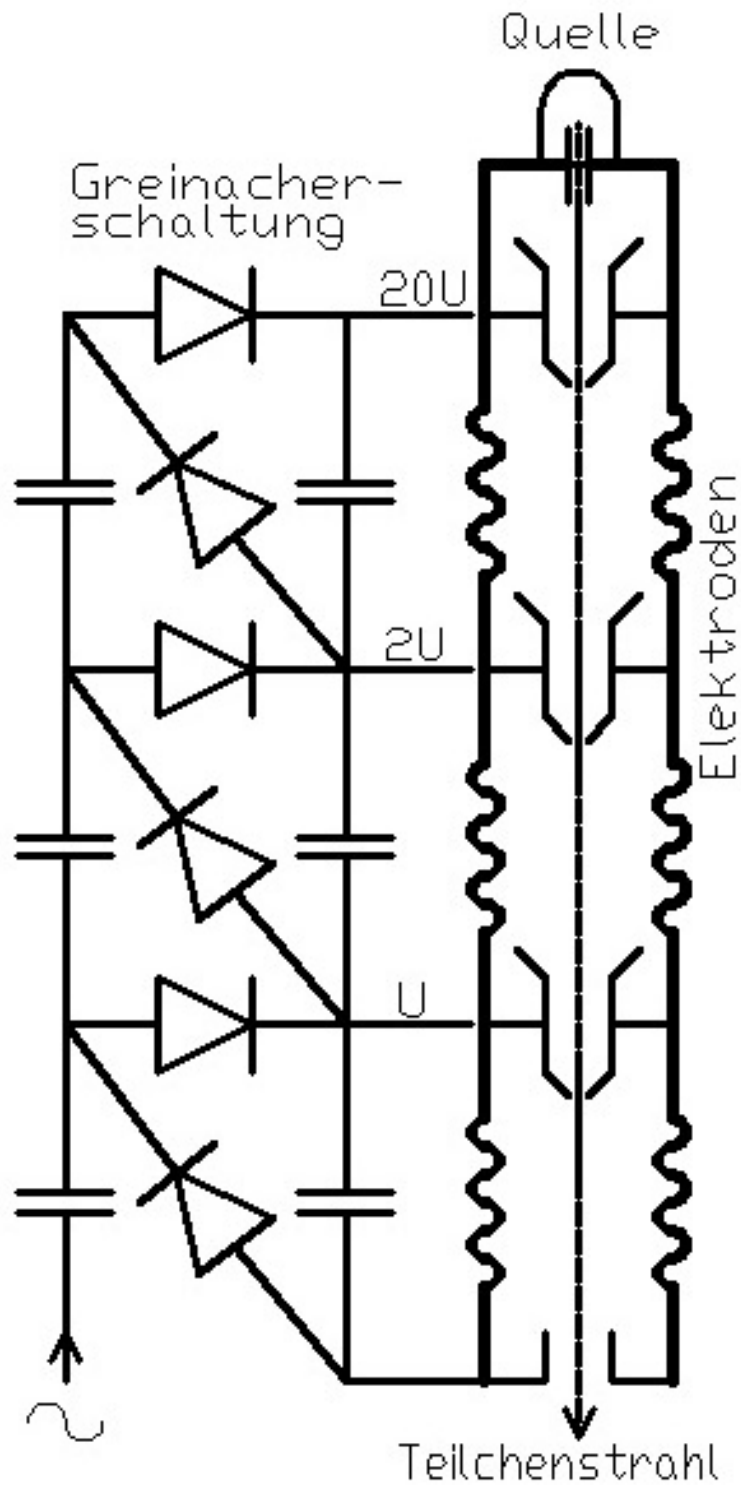


Figure C.1: Greinacher-style multiplier in combination with the 4 MV accelerator [38]. Each step of the electrical circuit is connected to a holey metal pot, which is placed below the source. As the ion beam passes through these pots it is accelerated by the electric field at the exit.

# Appendix D

## Beam line



## Beam line setup of the Dali-experiment

lengths in millimeter; drawing is not scaling reality

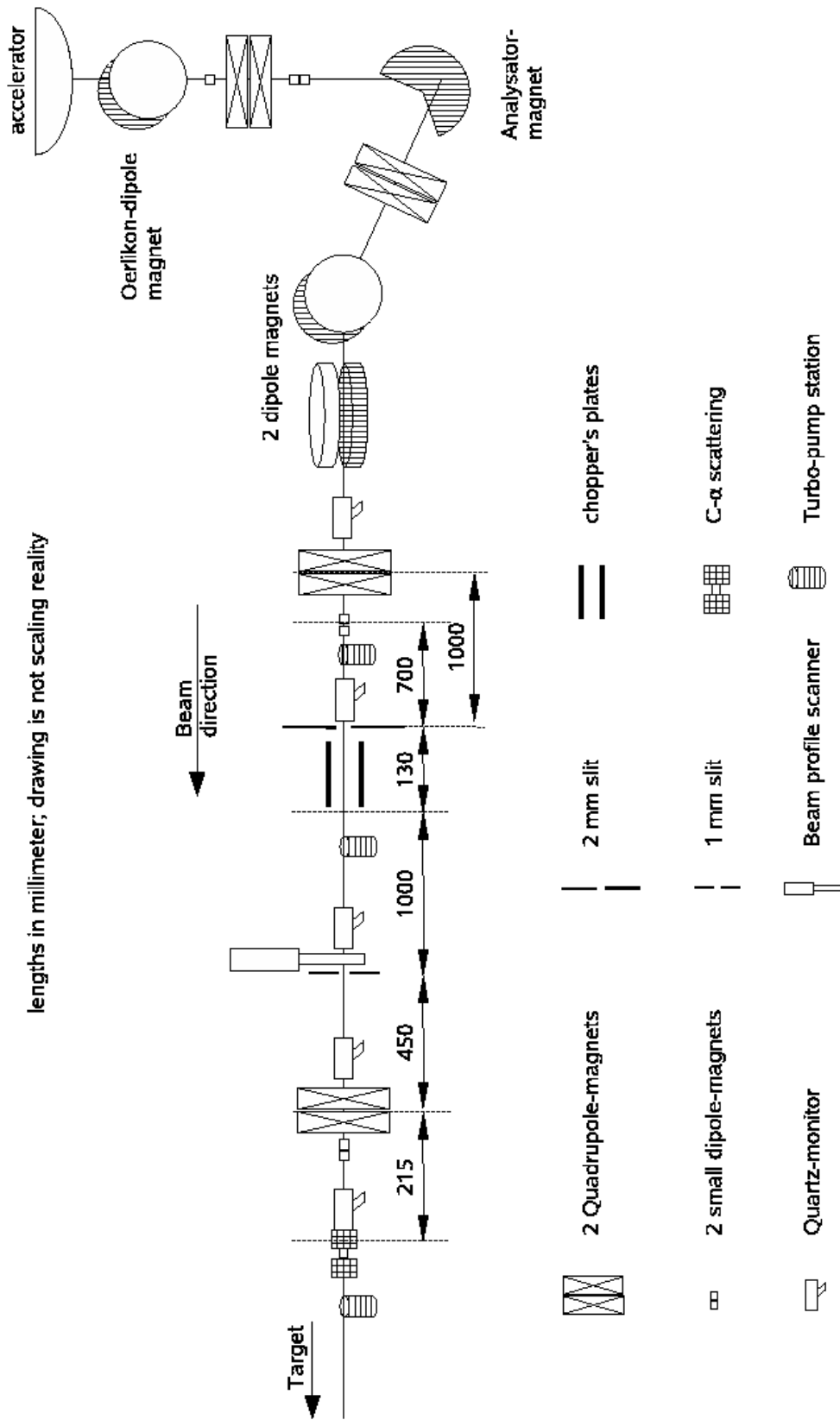


Figure D.1: Schematic drawing of the beam line.

# Appendix E

## Energy dependence of the time spectrum

The raw ADC spectrum of channel 8 as presented in figure E.1 is divided into eight slices where the region of interest of the expected events of the d- $\alpha$  capture corresponds to the slices 3 to 5. For the events of each slice the TDC spectrum is evaluated and presented in figure E.2 and E.3.

The TDC spectra of slice 1 and 2 show in comparison to the other spectra

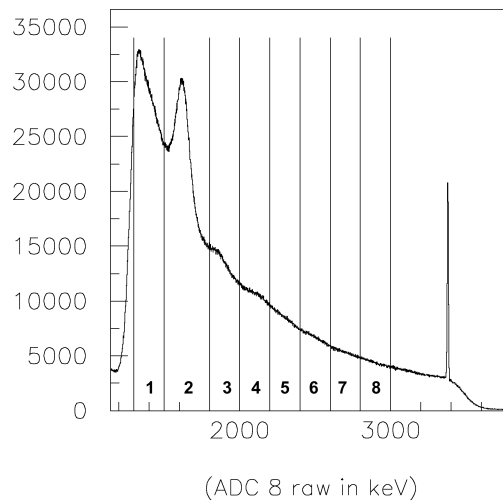


Figure E.1: *The raw energy spectrum of channel 8 has been cut into 8 slices. The TDC spectrum is then derived for each of the defined slices.*

that the main contribution to the gamma peak derives from the  $\alpha$ -O capture. In the region of interest only slice 5, which includes the resonance peak shows a clear signal as small bump before the dominant (n, $\gamma$ )-peak in the TDC spectrum. For the slices 3 and 4 the antecedent bump is not very pronounced.

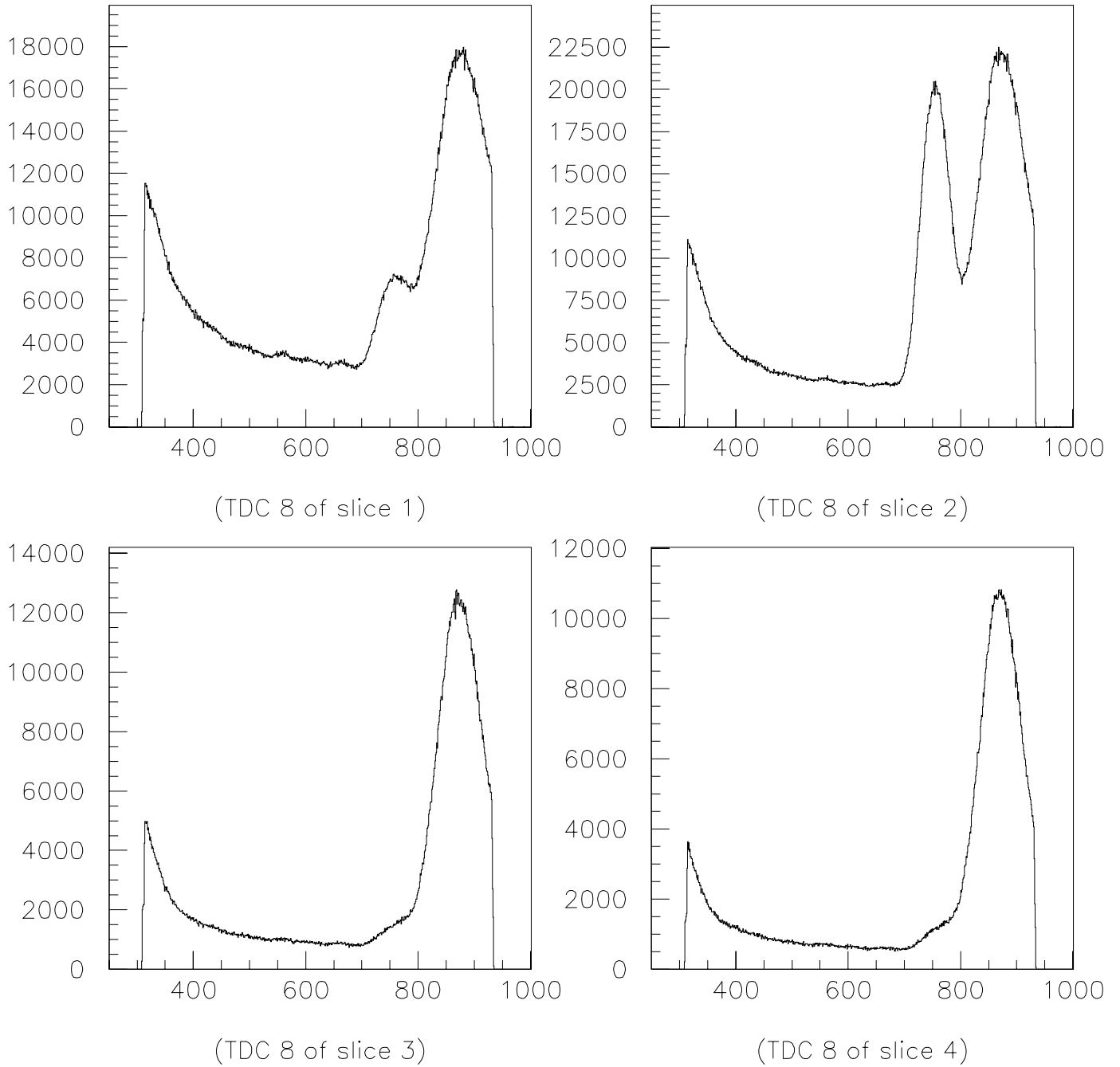


Figure E.2: *TDC spectra of ADC slices 1 to 4 of crystal No.8.*

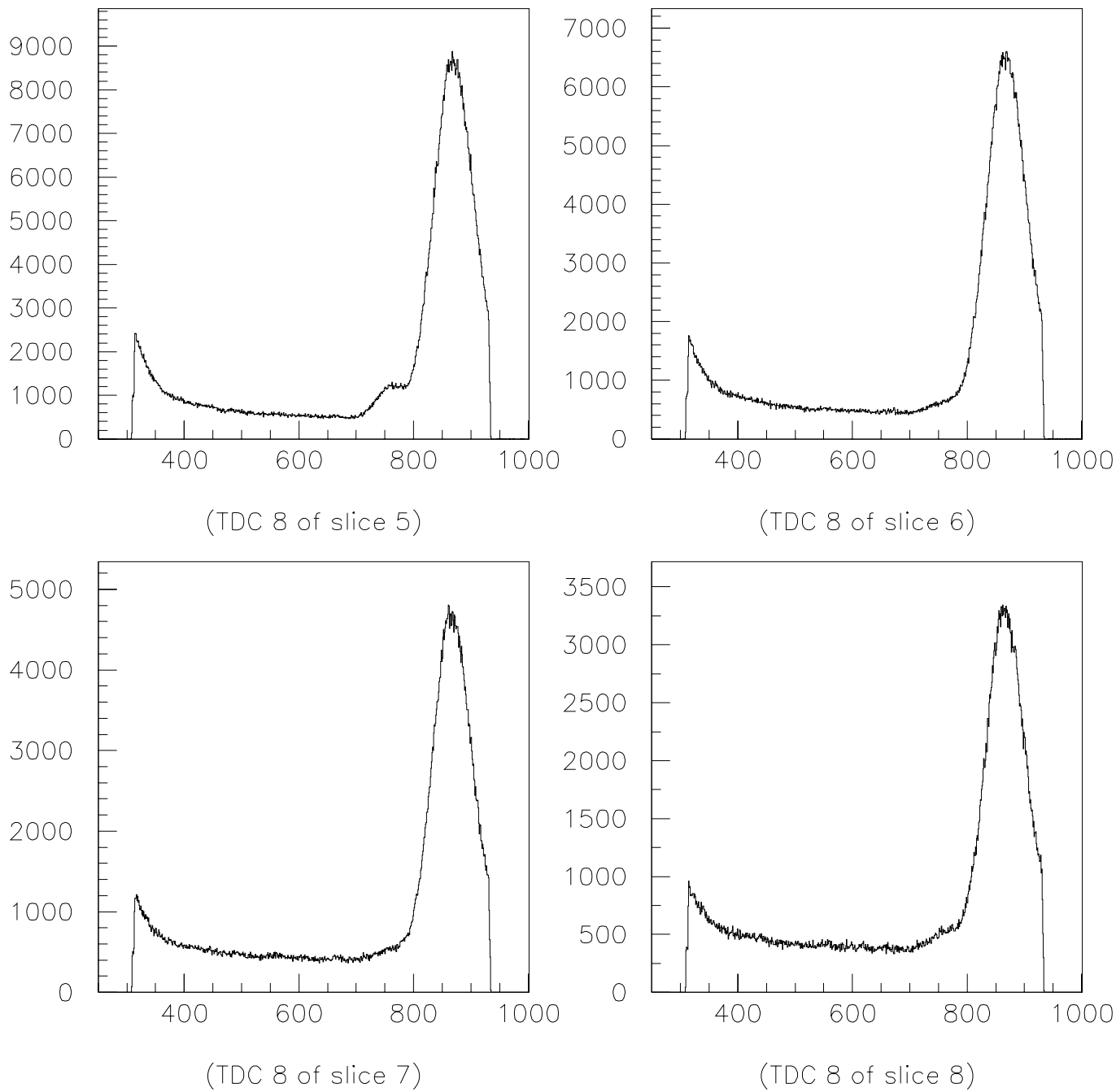


Figure E.3: *TDC spectra of ADC slices 5 to 8 of crystal No.8.*

# Bibliography

- [1] E. P. Hubble, *Proc. Nat. Acad. Sci.* **71**, 231 (1927)
- [2] A. A. Penzias and R. W. Wilson, *Ap.J.* **142**, 419 (1965)
- [3] D. Thomas, D. N. Schramm, K. A. Olive, and B. D. Fields, *Astrophys. J.* **406**, (1993) 569
- [4] N. Hata, R. J. Scherrer, G. Steigman, D. Thomas, and T. P. Walker, *Ap.J.* **458**, (1996) 637
- [5] A. Coc et al., *Astrophys.J.* **600** (2004) 544-552
- [6] K. M. Nollett, M. Lemoine, D. N. Schramm *Phys. Rev. C* **56**, 1144 (1997)
- [7] D. N. Spergel et al., *Astrophys.J.Suppl.* **148** (2003) 175
- [8] S. Burles, K. M. Nollett, J. N. Truran, and M. S. Turner, *Phys. Rev. Lett.* **82** (1999) 4176-4179
- [9] B. D. Fields and K. A. Olive *arXiv:astro-ph/9811183*
- [10] V. V. Smith, D. L. Lambert, and P. E. Nissen, *Astrophys. J.* **408**, (1993) 262
- [11] M. Asplund, D. L. Lambert, P. E. Nissen, F. Primas, and V. V. Smith *Astrophys. J.* **644**, (2006) 229-259
- [12] F. Hammache, A. Coc, J. Kiener et al. *New measurement of the cross section of the big bang nucleosynthesis reaction  $D(\alpha,\gamma)^6\text{Li}$  and its astrophysical impact, International Symposium on Nuclear Astrophysics -Nuclei in the Cosmos- IX, PoS(NIC-IX)013, June 2006*
- [13] K. M. Nollett, R. B. Wiringa, and R. Schiavilla *Phys. Rev. C* **63**, (2001) 024003
- [14] K. M. Nollet, *Private communication*
- [15] L.E. Marcucci, Kenneth M. Nollett, R. Schiavilla, R.B. Wiringa *arXiv:nucl-th/0402078v1*

- [16] J. Kiener et al. *Phys. Rev. C* **44**, 2195 (1991)
- [17] C. Angulo et al. *Nucl. Phys.* **A656**, 3-183 (1999)
- [18] R. B. Galli, *Ein Ionen-Beschleuniger für den symmetrischen 4 MV Kaskadengenerator, Dissertation 27. Februar 1961.*
- [19] E. Löffler, *Energie-Eichung, Diplomarbeit in Basel 8. Oktober 1975.*
- [20] D. Sacker, *Private communication; Energieeichung des Analysatormagneten, Maintenance protocol of the 4 MV, 29. Dezember 2003*
- [21] Glenn F. Knoll, *Radiation Detection and Measurement, second edition (1989)*
- [22] Particle Physics Booklet of 2006, particle data group
- [23] G. Heusser *Annu. Rev. Nucl. Part. Sci.* 1995. 45:543-90
- [24] R. G. H. Robertson, P. Dyer, R. A. Warner, R. C. Melin, T. J. Bowles, A. B. McDonald, G. C. Ball, W. G. Davies, and E. D. Earle *Phys. Rev. Lett.* **47**, 1867 (1981)
- [25] P. Mohr, V. Lölle, S. Wilmes, U. Atzrott, G. Staudt, J. W. Hammer, H. Krauss, and A. Oberhummer *Phys. Rev. C* **50**, 1543 (1994)
- [26] F. Cecil, J. Yan, C. Galowich *Phys. Rev. C* **53**, 1967 (1996)
- [27] B. Ya. Gorodilov et al., *Fiz. Niz. Temp.* **7**, 424 (1981)
- [28] With the kind permission of Advanced Research Systems, Inc. (April, 21 2008), *Private communication with Ravi Bains*
- [29] J. D. MacArthur, H. C. Evans, J. R. Leslie, and H.-B. Mak *Phys. Rev. C* **22**, 356 (1980)
- [30] C. M. Lederer and V. S. Shirley, *Table of Isotopes, seventh edition, John Wiley & Sons, Inc., 1978*
- [31] B. Grosswendt and E. Waibel *Nucl. Inst. Meth.*, **133** (1976) 25
- [32] S. Yalcin, O. Gurler, G. Kaynak, and O. Gundogdu *Appl. Radiat. Isot.* **65** (2007) 1179
- [33] Berger, M.J., Coursey, J.S., Zucker, M.A., and Chang, J. (2005), *ESTAR, PSTAR, and ASTAR: Computer Programs for Calculating Stopping-Power and Range Tables for Electrons, Protons, and Helium Ions* (version 1.2.3). [Online] Available: <http://physics.nist.gov/Star> [2008, April 26]. National Institute of Standards and Technology, Gaithersburg, MD.

- [34] P. Bauer, W. Käferböck, V. Necas, *Nucl.Instrum.Methods Phys.Res.* **B93**, 132
- [35] W.A. Wenzel, W. Whaling, *Phys.Rev.* **87**, 499-503 (1952)
- [36] ICRU (1993), International Commission on Radiation Units and Measurements, *ICRU Report 49, Stopping Powers and Ranges for Protons and Alpha Particles*
- [37] K. M. Nollett, *Private communication*
- [38] D. Sacker, *Picture reproduced with the courtesy of Daniel Sacker, Uni Basel, 2007*
- [39] D.R. Tilley, H.R. Weller and C.M. Cheves *Nucl. Phys. A* **A564**, No.1 (1993)

# Curriculum vitae

Name	Giuseppe A. Testa
Geburtsjahr	1975
1991-1995	Wirtschaftsgymnasium in Basel
1995	Matura Typus E
1995-2002	Studium in Physik an der Universität Basel
2002	Diplom in Experimentalphysik Diplomarbeit: "Measurement of the tensor and vector analyzing power of the radiative d-p capture reaction"
2002-2007	Dissertation an der Universität Basel Titel: "Measurement of the Total Cross Section of the ${}^2\text{H}(\alpha,\gamma){}^6\text{Li}$ Radiative Capture Reaction"
2008	Doktoratsexamen
2008-	Eidgenössisches Nuklearsicherheitsinspektorat ENSI (ehem. HSK)

## Ausbildung

Meine Ausbildung an der Universität Basel verdanke ich folgenden Dozenten:

PD Dr. Jürg Jourdan  
PD Dr. Daniela Kiselev (geb. Rohe)  
Prof. Dr. Bernd Krusche  
PD Dr. Heini Mühry  
Prof. Dr. Dr. h.c. Ingo Sick